Available on CMS information server

CMS NOTE-2007/028

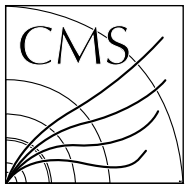

The Compact Muon Solenoid Experiment

CMS Note

Mailing address: CMS CERN, CH-1211 GENEVA 23, Switzerland

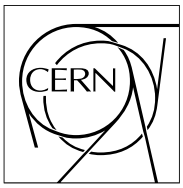

15 November 2006

Laser monitoring system for the CMS lead tungstate crystal calorimeter

M. Anfrevilleb, D. Bailleuxa, J.P. Bardb, A. Bornheima, C. Bouchand, E. Bougamont, M. Boyer, R. Chipaux, V. Daponte-Puill, M. Dejardin*, J.L. Faure, P. Gras, P. Jarry, C. Jeanney, A. Joudon , J.P. Pansart, Y. Penichot, J. Rander, J. Rolquin, J.M. Reymond, J. Tartas, P. Venault, P. Verrecchia , L. Zhang, K. Zhu, R.Y. Zhu

Abstract

We report on the multiple wavelength laser monitoring system designed for the CMS lead tungstate crystal calorimeter read-out with avalanche photodiodes (Barrel calorimeters) and vacuum phototriodes (End Cap calorimeters). Results are presented for the test beam performance of the system designed to achieve 0.5

1. Introduction

Lead tungstate ($PbWO_4$) crystals were chosen for the 75 848 channel electromagnetic calorimeter (ECAL) currently under construction for the Compact Muon Solenoid (CMS) experiment at the CERN LHC [1]. Geometrically, the ECAL consists of a cylindrical barrel containing 61 200 crystals, closed at each end with end-caps, each containing 7324 crystals. The barrel is made up of 36 supermodules (SM), each with 1700 crystals arranged in a quasi-projective geometry (off-set 3° from the interaction point) and read-out with avalanche photodiodes (APD, two per crystal). Each SM [1] is composed of 4 modules, starting from the interaction point (pseudorapidity $\eta = 0$): module 1 (500 crystals), module 2 (400 crystals), module 3 (400 crystals) and module 4 (400 crystals) reaching the outer edge ($|\eta| = 1.479$). The end-caps are made up of two Dees, each with 3 662 crystals arranged quasi-projectively and read-out with vacuum phototriodes (VPT, one per crystal). The Dees are assembled with supercrystals (SC) of typically 25 (5 x 5) crystals.

The choice of lead tungstate was based upon the crystal's high density and its radiation hardness: the scintillation light mechanism is not affected by irradiation. However, the optical transmission at the scintillation wavelengths is affected by the production of color centers under ionizing irradiation [2][3]. Furthermore, spontaneous annealing of the color centers occurs at room temperature. This leads to a transmission recovery, which is evident when the crystals are not irradiated such as during machine-fill gaps between physics collision runs. Light transmission at any moment of time is the result of an equilibrium between the rates of color center production and their annealing. Crystals produced for the ECAL are the result of a long R&D process to optimize doping and production stoichiometry to reduce the scale of the variations in light transmission during an LHC collision running period (at luminosities of 10^{34} cm^{-2} s^{-1}) to less than 6% for barrel crystals (typical dose rates of 0.15 Gy/h) and less than 20% for the end-cap crystals at $|\eta| = 2.5$ (typical dose rates of 1.9 Gy/h).

The importance of measuring the variations of the optical transmission of the crystals at LHC can be illustrated by considering the scintillation signal S_i for a single channel (i) at the emission wavelength λ, which can be factorized approximately as follows:

$$S_i(E, \lambda) = [N(E) \cdot LY_i(\lambda)] \cdot Tr_i(\lambda) \cdot [A_i \cdot QE_i(\lambda) \cdot M_i(\lambda)] \ ,$$

where the first term includes the shower deposition N(E) and the scintillation light yield factor LY, the second term is the optical transmission $Tr_i(\lambda)$ at the given wavelength, and the third term regroups the geometrical acceptance A, the quantum efficiency QE, and the gain M of the photodetector. Although the first term is unaffected by irradiation at LHC, the second, the optical transmission $Tr_i(\lambda)$, is affected and directly disturbs the energy measurement. The third term can be controlled by using radiation hard photodetectors and by measuring the electronics gain. Uncertainties in the relative measurement of the optical transmission, from crystal to crystal, contribute directly to the energy resolution. The energy resolution and uniform response of the calorimeter are critical to the discovery of a Higgs boson via its decay into two photons, where the discovery potential is driven by the experimental resolution. The energy resolution of the barrel calorimeter was measured in a test beam with electrons from 20 to 250 GeV, and the result [4] is consistent with expectations: a mean stochastic term of $2.8\%/\sqrt{E}$ and a mean constant term of 0.3%. The final calibration of the ECAL will be achieved using physics events collected over days or weeks, depending upon the calibration process, but the energies need to be corrected for the optical transmission variations occurring during each LHC collision run. The goal of the system described in this

paper is to provide these corrections, while achieving ≤ 0.2% relative inter-channel precision in the transmission measurements, and to ensure the stability of the corrections at that level over periods of a month for all of the 75 848 channels of the full ECAL.

Two options have been used previously for frequent *in situ* light transmission measurements of individual crystals in calorimeter systems with up to ~10 000 crystals: radioactive sources or external light injection. Radioactive sources are interesting in that they monitor the product of the light yield and transmission terms. Unfortunately, the relatively high noise level ~ 40 MeV of the ECAL barrel avalanche photodiode (APD) and its associated electronics does not allow such a solution. Light injection systems have generally used xenon flash lamps or light emitting diodes (LED) [5,6,7,8,9] producing photodetector signals up to about 35 GeV electron equivalent; they have proven their efficiency in detecting photodetector failures [7], correcting detector gain shifts [6], and detecting non-linear response in electronics [8]. This approach, using a LED to externally inject light at 660 nm successfully followed irradiation induced light losses on a CMS prototype 7x7 crystal matrix in test beam studies performed at CERN in 1996 [10]. These studies underlined the importance of injecting light nearer the scintillation peak wavelength.

However, these light injection levels are insufficient at LHC, where we want to be able to measure the response from equivalent energies of 13 GeV up to 1.3 TeV on an array of 75 848 crystals. This requirement has led us to design a laser light injection system to cover the required dynamic range. The design precision was achieved by placing both a light-mixing step and a stable reference monitor sufficiently close to the final light injection at the crystal.

In this paper, we report on the design, installation at the detector level, and performance of the ECAL laser monitoring system. The system has been used during test beam studies of ECAL barrel supermodules; results relevant to the performance of the laser monitoring system are also presented here.

2. Laser monitoring system

2.1. Overview

The major components of the laser monitoring system presented in this paper are shown schematically in Fig.1. Laser light is produced at a source (installed in the CMS underground service cavern USC55) either at the principle wavelength of 440 nm (blue), near the Y doped $PbWO_4$ scintillation emission peak, or at 796 nm (near IR), only weakly sensitive to color center production, which is used as a cross-check of gain variations. The laser light pulses are directed to individual crystals via a multi-level optical fiber distribution system: a) a fiber-optic switch at the source directs the pulses to a selected calorimeter element (altogether 88 elements: 72 half SMs, and 16 quarter Dees); b) a primary optical fiber distribution system transports the pulses over a distance of 95 to 130 m to each calorimeter element mounted in CMS (located in the experimental cavern UXC55), and c) a two-level distribution system mounted on the detector sends the pulses to the individual crystals. The total attenuation of the light distribution system is measured to be 69 dB (laser source to crystal front face).

The basic principle of operation is illustrated for the barrel geometry in Fig. 1: laser pulses transported via an optical fiber are injected at a fixed position at the crystal's front face, the injected light is collected, as for scintillation light from an electromagnetic shower, with the

pair of APDs glued to the crystal's rear face. This design ensures that the crystal's optical transmission is measured in the region of interest, although the optical light path is somewhat different from that taken by scintillation photons generated along the shower within a crystal. The underlying principle is similar for ECAL end-cap, however there the calorimeter design based on SC units [1] does not permit front face injection; in this case, laser light is injected at a corner of each end-cap crystal's rear face, and the light is collected (as for scintillation) via a VPT glued on the crystal's rear face. Since the optical transmission depends upon light path, the ratio of scintillation to laser response differs between barrel and end-caps.

In order not to interfere with ECAL performance during physics collisions at LHC, the laser pulses are injected during 3.17 μs gaps foreseen every 88.924 μs in the LHC beam structure [11]. Running the laser source at 100 Hz means injecting laser pulses in 1% of the available gaps. The laser monitoring system independently measures the injected light for each pulse distributed to a group of typically 200 crystals using pairs of radiation hard PN photodiodes read-out via dedicated front-end electronics. The crystal optical transmission corrections are made using the ratio of the crystal's APD (VPT for the end-caps) response normalized by the associated group's PN response. The system is foreseen to continuously cycle over the calorimeter elements, giving a transparency measurement every 20 to 40 minutes. The components of the monitoring system mounted on the calorimeter are designed to be radiation hard; full LHC luminosity running over 10 years, depending upon angle, will expose them to a total integrated dose of typically 3 kGy, and a neutron fluence of $2x10^{13}$ n/cm^2 [12]. Irradiation test results are discussed in section 3.

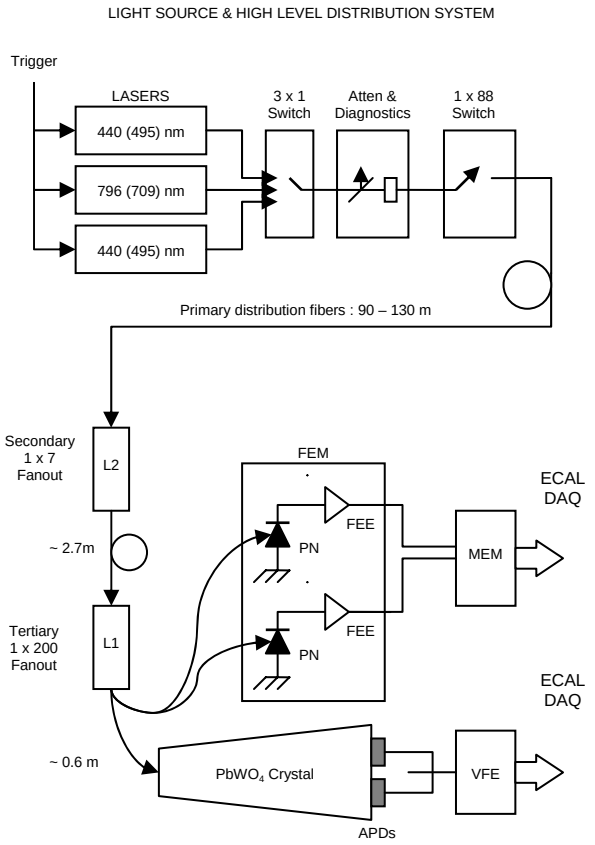

Figure 1. *Schematic of the laser monitoring system: laser pulses generated at the source (above) are distributed to individual calorimeter elements via one of 88 primary fibers. The pulses are then distributed on the detector via a two level fan-out system, injecting the light into groups of typically 200 crystals (bottom) and in parallel into associated pairs of reference PN photodiodes.*

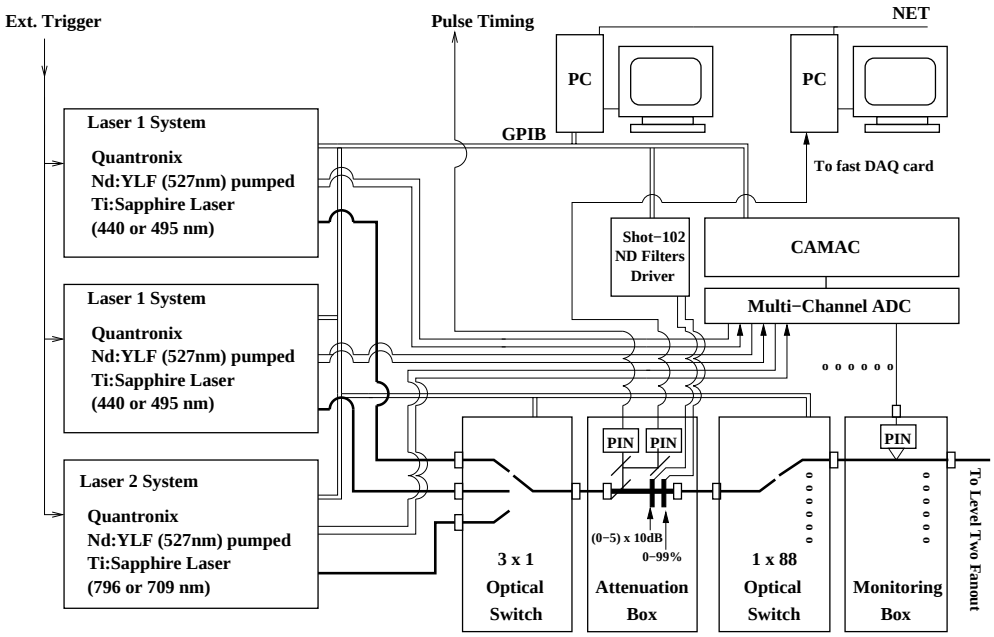

Figure 2. *Schematic diagram of the monitoring light source consisting of three lasers.*

2.2. Multiple wavelength monitoring light source and high level distribution system

Since the monitoring light source has been presented elsewhere [13], only the design requirements, the essential characteristics and performance are reviewed here. The laser source specifications and its environmental requirements are listed below:

- Operation duty cycle: 100% during LHC data taking periods (expected to be about 5000 hours/year).
- Two operating wavelengths: 440 nm (blue) and 796 nm (near IR).
- Spectral contamination: $< 10^{-3}$.
- Pulse energy (E_{pulse}): 1mJ at the source for a dynamic range up to an equivalent deposition of 1.3 TeV in a crystal with 69 dB attenuation in the distribution system.
- Pulse width (Γ_{pulse}): < 40ns FWHM to match the ECAL readout.
- Pulse jitter: < 4 ns (24 hours), < 2 ns (30 min).
- Pulse rate: ~ 100 Hz.
- Pulse to pulse instability: < 10% of E_{pulse}.
- Clean room class: better than 10 000 to protect laser optics.
- Temperature stabilization: ±0.5° C and humidity <60%.

The monitoring light source consists of three laser systems (two “active” and one “spare”) each equipped with diagnostics, shown schematically in Fig. 2. Each laser system mounted on its optical bench, see Fig. 3, consists of two lasers: 1) a Quantronix [14] model 527DQ-S Q-switched Nd:YLF pump laser used to excite the Proteus, which delivers pulses up to 20 mJ at 527 nm, and 2) a Quantronix [14] custom made Proteus UV(SHG) dual wavelength Ti:Sapphire laser, supplying up to 1 mJ pulses at rates up to 100 Hz. Laser characteristics are summarized in Table 1. The additional wavelengths of the two sources, 495 nm (green) and 706 nm (red), allow systematic studies of the calorimeter’s evolution. Typical pulse shapes are shown in Fig. 4. The spectral contamination was confirmed to be $< 10^{-3}$ with a high resolution monochromator, Oriel MS257.

Table 1. Monitoring Light Source Laser Characteristics.

Characteristics	QUANTRONIX [14] Laser				
	Nd:YLF	Ti:Sapphire 1		Ti:Sapphire 2	
Wavelength λ (nm)	527	440	495	796	706
Pulse energy (mJ)	20	1	0.5	1.5	0.42
Pulse width (ns)	100-170	25-30	40-50	25-30	30

The output of any one of three sources is selected with a DiCon [15] 3x1 fiber-optic switch. The output intensity is adjusted by two attenuators in series: a linear attenuator allows 1% steps down to 13 GeV and a logarithmic attenuator increases the dynamic range. Both are controlled by computer, allowing pulse intensity scans to measure linearity. Pulse energy, FWHM and timing of the lasers are measured by a slow monitor using PIN photodiodes and an Agilent Digital Sampling Oscilloscope (2Gs/s) with a sampling rate of about 1 Hz. An Acqiris DP210 digitizer card (2Gs/s) is inserted between the two optical switches; it functions locally as a fast monitor, and is capable of analyzing laser pulses up to 100 Hz. The attenuated pulses are sent to the selected calorimeter element's primary distribution fiber via a computer controlled DiCon [15] 1x88 fiber-optical switch.

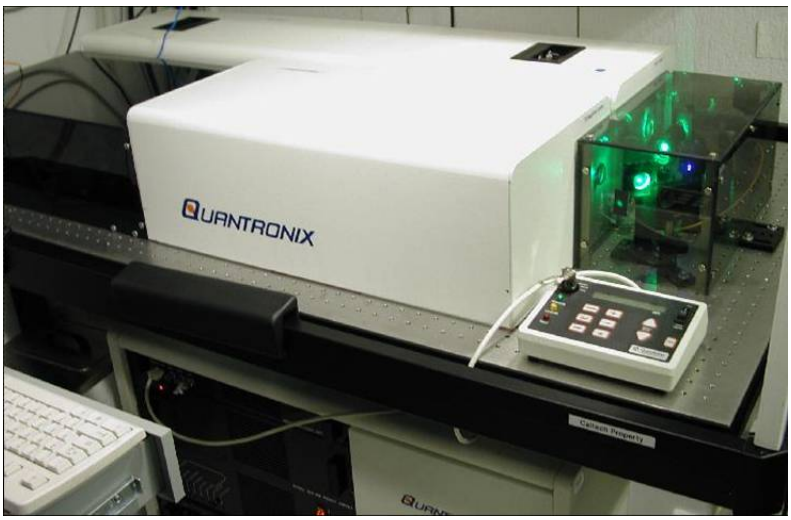

Figure 3*. The monitoring system multiple wavelength light source (shown installed at CERN H4 test beam area).*

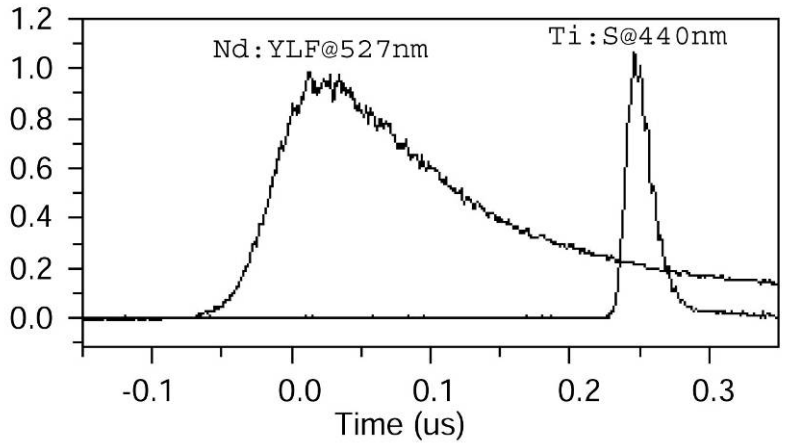

Figure 4. *Measured pulse shapes for the monitoring light source Nd:YLF pump laser at 527 nm and the Ti:Sapphire laser at 440 nm.*

2.3. Online laser pulse-width diagnostics: fast switched-capacitor digitizer

The shaping time of the front-end amplifier attached to the crystal's photodetector (e.g. avalanche photodiodes APD for the ECAL barrel) is ~ 50 ns, whereas the front-end amplifier of the reference PN photodiodes (see section 2.6.1) used to monitor the laser pulses required a shaping time of ~1 μs. Therefore the measurement of the crystal transparency using the ratio of crystal's photodetector response versus the PN photodiode is affected by variations of the laser pulse-width. Since the intrinsic stability of the Ti:S laser pulse width (Γ_{pulse}) is about 3%, or 1 ns for a 30 ns laser pulse, a fast switched-capacitor digitizer was used to measure both the laser pulse-width and its timing to allow for corrections (discussed in section 5.3).

In order to perform this task a PIN photodiode with fast shaping is placed just before the attenuator (see Fig. 2) and its signal is sent via a video amplifier (band width > 400 MHz) to the readout. A CAEN V1729 4 channel 12 bit 2 GHz switched-capacitor digitizer is used to digitize each laser pulse. This VME module is based on the MATACQ (analog matrix) chip developed by LAL and DAPNIA [16]. The typical reconstructed laser pulse width precision is 300 ps, which is largely sufficient for the corrections discussed later.

2.4. Monitoring light distribution system

The monitoring light distribution system receives laser pulses from the fiber-optic switch at the source and injects them into the individual crystals via a three level optical fiber distribution system outlined previously: primary fibers carry the pulses to the selected calorimeter element (e.g. half SM), a secondary (L2) fan-out mounted on each calorimeter element distributes the pulses to 4 or 5 tertiary (L1) fan-outs, each serving typically 200 crystals. The general layout is illustrated in Fig. 5 for a barrel SM, where a slight asymmetry between the two secondary chains is apparent due to the additional 100 crystals of module 1. Each of these levels is described in this section. Multi-mode step index fibers were selected for use throughout the distribution system due to their large numerical aperture (NA), large diameter, and low cost; the characteristics are summarized in Table 2 for each level. Efficient source coupling has made this fiber type a common choice in laser power transport applications where distances are < 2 km, or where dispersion is not critical.

All of the distribution system components are mounted on the SM's front face, where throughout this paper the expression "front face" refers to the face closest to the LHC interaction point. Individual crystals are accessed via slots in the front face. The primary fibers must access the element from the end of module 4 as shown in Fig. 6. The layout on a typical module is shown in Fig. 7. Installation of these components is addressed in section 4.5.

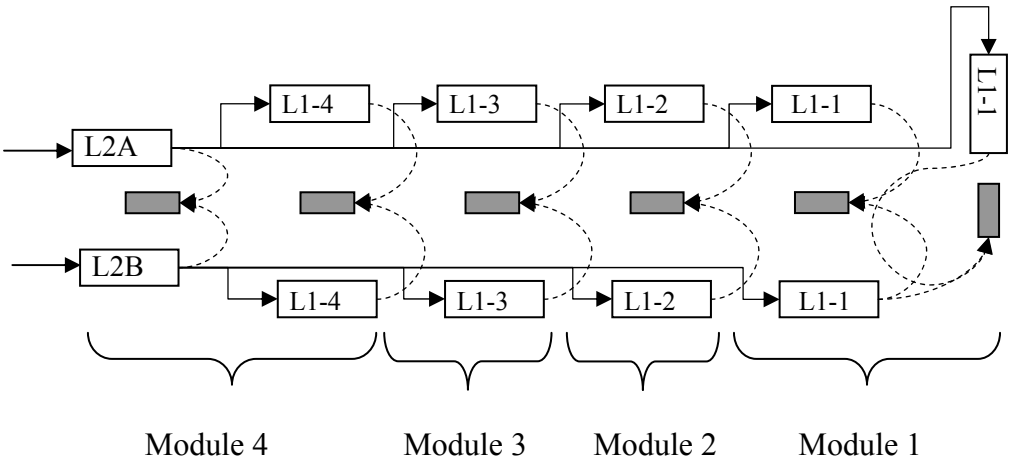

Figure 5. *Schematic of the ECAL barrel SM light distribution. Laser pulses (entering at left) are sent to either one of two secondary (L2) fan-outs L2A or L2B, and are distributed to crystals along the left or right half of the SM's longitudinal axis via 4 or 5 tertiary fan-outs located in each of the four modules. The FEM units housing pairs of reference PN photodiodes monitoring each fan-out are shown shaded.*

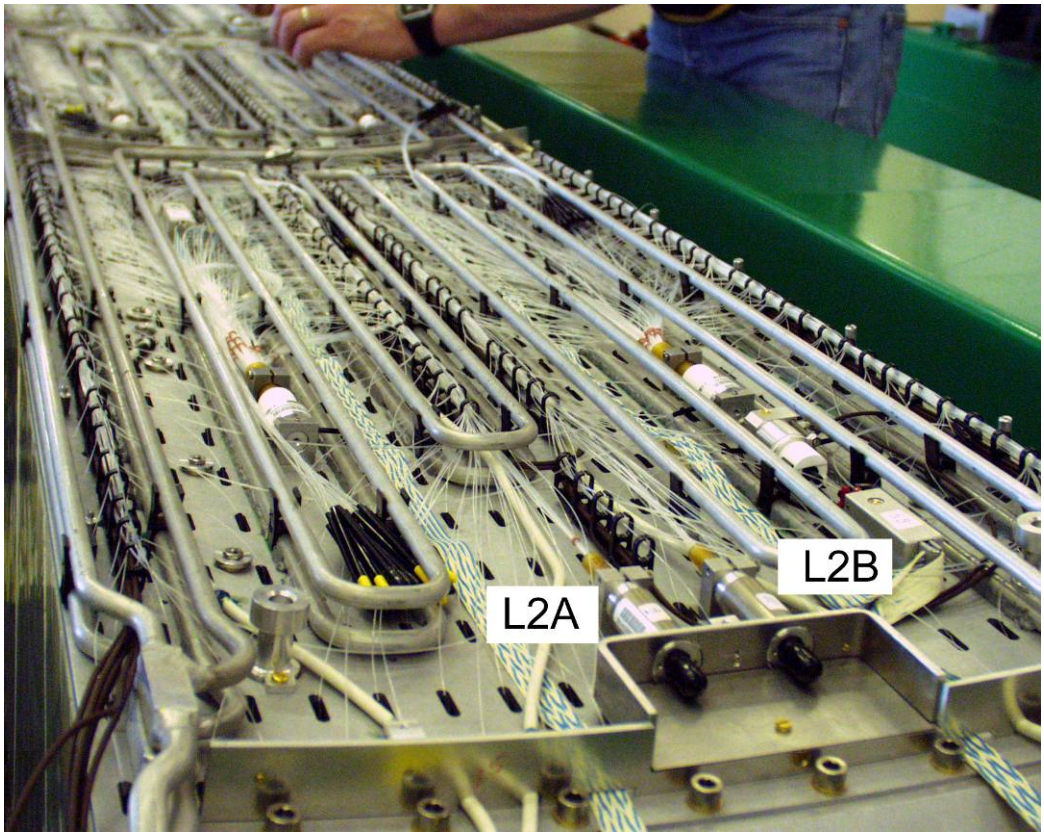

Figure 6. *Module 4 (outermost) module of an ECAL barrel SM (front cover removed) showing the monitoring components mounted on the front face along with cooling tubes (LHC beam-line overhead here). Laser light enters the SM via primary fibers connected to the two fan-outs (L2A & L2B) visible at the lower edge.*

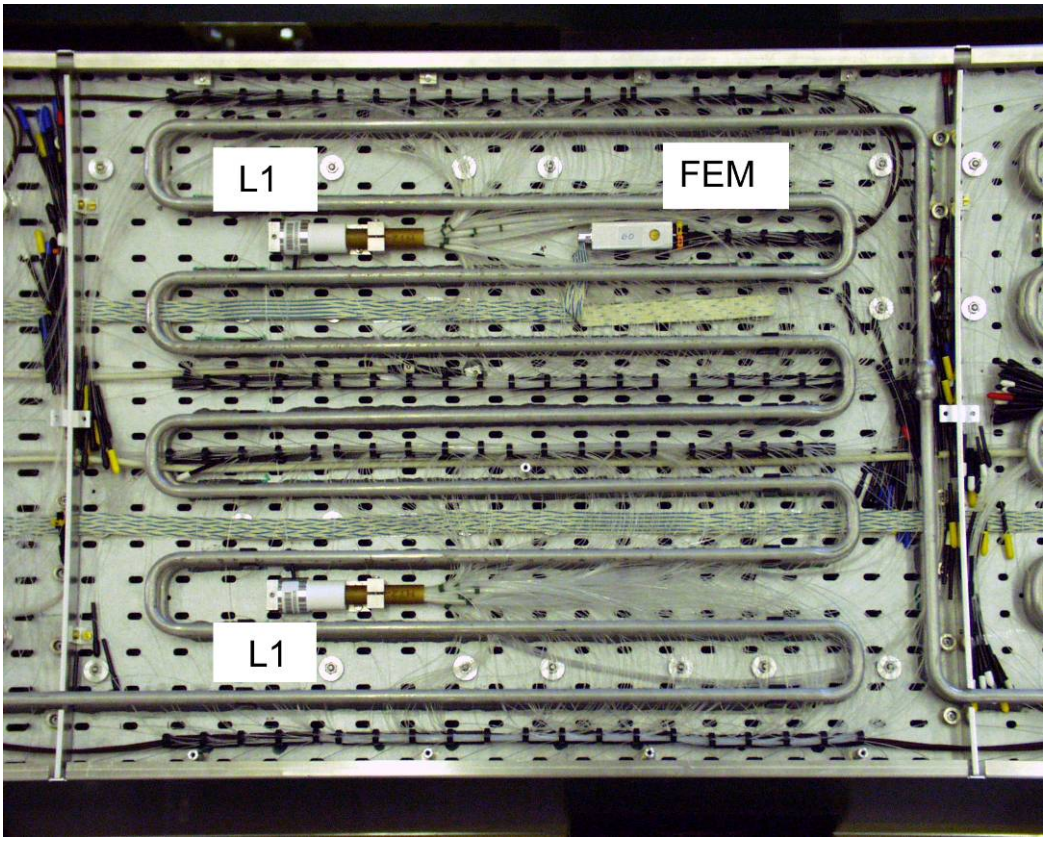

Figure 7. *Typical installation of monitoring components on a SM module front face (here Module 2): two tertiary (L1) fan-outs are visible (top and bottom of center); the optical fibers access the crystals though the slots. The rectangular box (top right) is the FEM unit.*

Table 2. Monitoring light distribution system optical fiber types.

Distribution System Application	Multi-mode step-index fiber type	Core/cladding/ sheath(s) Ø (µm)	NA	SpecTran Identification
Primary distribution	silica-silica-polymer-Tefzel®	365/400/ 430/700	0.22	HCG-M0 365T High OH^-
Secondary 1:7 fan-out (L2)	silica-silica-polymer-Tefzel®	365/400/ 430/700	0.22	HCG-M0 365T High OH^-
Tertiary 1:240 Fan-out (L1) ECAL barrel	silica-polymer-Tefzel®	200/230/ 500	0.37	HCP-M0 200T Low OH^-
Tertiary 1:240 Fan-out (L1) ECAL end-cap	silica-silica-polymer-Tefzel®	200/240/ 260/375	0.22	HCG-M0 200T High OH^-

2.4.1. Primary distribution fibers.

SpectTran silica-silica core optical fibers with a hard polymer cladding and an ETFE fluoropolymer resin jacketing (Tefzel® Dupont) are used for the primary distribution. The primary fibers are arranged in 6-fiber trunk cables (9mm diameter including a protective sheath and a central core). The polished extremities are glued in ST type connectors. Individual ECAL barrel primary fibers are 95 m long and are installed without cutting/splicing. However, the 130 m long ECAL end-cap primary fibers must be installed in two steps; a 105 m length from the source to the detector is spliced after installation to a 25 m length pre-installed on the end cap magnet yoke. The two ends to be spliced are cleaved and glued with epoxy [17] on a 5x50 mm optical glass plate using a SEDI [18] developed

"Laboptic" fiber splice (loss 0.1 to 0.4 dB). The additional length of the end-cap primary fibers allows their movement during opening of the CMS detector for maintenance. Typical attenuation loss in the primary fibers is 9 dB.

2.4.2. Secondary (L2) fan-out.

The secondary fan-out mounted at the edge of a calorimeter element is designed to receive the primary fiber (ST connector) and distribute the laser pulses to the tertiary fan-outs. Two secondary fan-outs are required for an ECAL barrel SM and four secondary fan-outs are required for an ECAL end-cap Dee.

The light uniformity requirements between outputs at this level are satisfied at the ±1.5% level, so a simple reflective light splitter is used. The assembly components shown in Fig. 8 consist of the light splitter mounted in a protective housing and a 7-fiber optical fan-out. The splitter is an air-filled aluminized glass light guide 25 mm long with a 1.7 mm x 1.7 mm^2 inner section. Laser pulses enter the end of the light guide via an ST connector which centers fiber. The fiber's numerical aperture is sufficient to ensure multiple reflections along the guide. Centered at its far end is the 7-fiber fan-out, which receives and distributes the pulses. The fan-out consists of 7 silica-silica core fibers (ref. Table 2) hexagonally packed and glued [17] into a 6 mm long molded centering piece, which is inserted and glued [17] into a 50 mm long fiber bundle tube (8mm outer diameter, O.D.). A 1.9 mm long narrow collar (4 mm O.D.) on the centering piece's face ensures its mechanical positioning in the light splitter assembly. Both the centering insert and the bundle tube are made of polyetherimide (Ultem® GE Plastics). The polished face of the bundle tube assembly can be seen in Fig. 12. Fiber lengths depend upon where the tertiary fan-outs are located: a) barrel fan-out fiber lengths are given in Table 3, b) end-cap fan-out fibers are all 1500 mm long. The barrel secondary (L2) and tertiary (L1) fan-out optical fiber lengths are designed (propagation speed 5ns/m) to match the differences in delay time for gammas or relativistic electrons arriving at the center of each module from the CMS interaction point.

Optical fibers are glued [17] into ferrules which are assembled from similar elements for both secondary and tertiary level fan-outs. A "standardized" 12 mm long molded polyetherimide ferrule end (2.5 mm O.D.) is joined to an extruded polyamide tube (2.5 mm O.D.) which is cut to length depending upon the application. In the secondary fan-out case the assembled ferrule length is 23 mm and the finished fiber end is polished. Effective light loss from the secondary fan-out's input to the entry of each of the individual tertiary fan-outs is -17 dB.

Table 3. ECAL barrel secondary (L2) 7-fiber fan-out specifications
(Total fiber length includes the bundle tube & ferrule)

Module	L2 Total Fiber length	L1 Fan-out Type Served
1	2573 $^{-0}/_{+12}$ mm	L1-1
2	2723 $^{-0}/_{+12}$ mm	L1-2
3	2723 $^{-0}/_{+12}$ mm	L1-3
4	3123 $^{-0}/_{+12}$ mm	L1-4

***Figure 8**. Secondary fan-out light splitter shown fully assembled above (light injection from right), and opened below with the 25 mm long light guide (1.7x1.7 mm^2 inner section) removed prior to bonding.*

2.4.3. Tertiary (L1) fan-out.

The tertiary fan-out is designed to receive the laser pulses from the secondary fan-out and distribute the light to the individual crystals. Nine tertiary fan-outs are required for an ECAL barrel super module, and 20 fan-outs are required per ECAL end-cap Dee. Different optical fiber types were chosen for the ECAL barrel and end-cap cases (see Table 2): for the barrel, the shorter fiber lengths and significantly lower expected dose at LHC (discussed in sect. 3.1) allows the use of lower cost silica-polymer core fiber, whereas for the end-caps, the longer length and higher expected dose lead us to chose silica-silica core fiber. The minimum allowed bending radius is critical to the installation in the limited space available: ≥16 mm for the silica-polymer core fiber selected and ≥ 14 mm for the silica-silica core fiber.

The stability of the relative transmission between the ~200 crystals and the reference PN photodiode pair served by a common tertiary fan-out is critical to the precision of the transparency measurements. The use of an integrating sphere at this fan-out level is essential to improve stability for light pulses from a coherent source, where speckle effects can introduce transient variations between fibers due to effects such as small displacements. The limited 25 mm space allowed between the SM front face and the front cover constrains the design and lead us to the use of a 12 mm inner diameter I.D. thermoplastic (Spectralon® [19]) diffusing sphere. The tertiary fan-out assembly shown in Figs. 9 and 10 consists of the diffusing sphere into which the secondary fiber's ferrule is inserted at 90° to the axis of the 240-fiber optical fan-out, all of which is mounted in a mechanical housing. Once installed, the faces of the ferrule and fan-out are recessed by 0.5 mm and 0.1 mm respectively with respect to the sphere's I.D. The fiber length and free-end ferrule length are specific to the location of the crystals served (e.g. crystal inclination in the SM increases with η). Tables 4 and 5 give the specifications for the ECAL barrel and end-cap fan-outs, respectively. Typical fan-out uniformity gives an RMS spread of 2.4% over the 240 fibers; measurements are discussed in section 4.1. Measured effective loss from the tertiary fan-out's input to an individual crystal's face is -39 dB.

***Figure 9**. The ECAL barrel tertiary (L1)240-fiber optical fan-out assembly. The fan-out inserts into a 12 mm I.D. diffusing sphere (shown opened here). Light is injected at 90° to the fan-out's axis via the ferrule.*

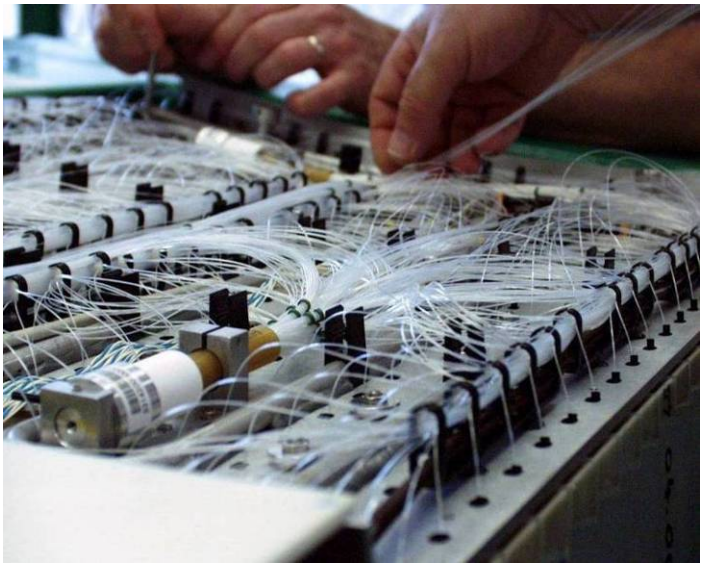

***Figure 10.** The ECAL barrel tertiary (L1) fan-out and its diffusing sphere assembly shown installed on a SM front face.*

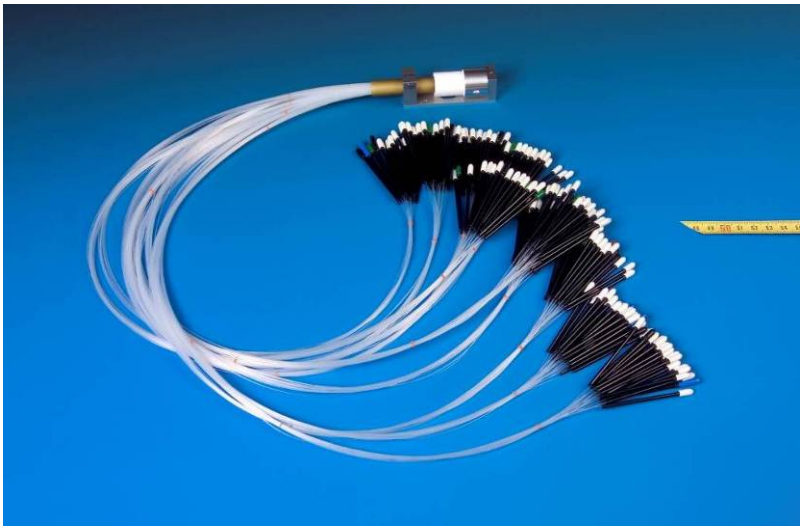

***Figure 11.** The ECAL barrel tertiary (L1) 240-fiber fan-out. The fibers are grouped to facilitate their installation.*

Table 4. ECAL barrel tertiary (L1) 240-fiber fan-out specifications

Fan-out Type	Total fiber length	Ferrule length
L1-1	493 $^{-0}/_{+12}$ mm	23 mm
L1-2	500 $^{-0}/_{+12}$ mm	30 mm
L1-3	711 $^{-0}/_{+12}$ mm	41 mm
L1-4	727 $^{-0}/_{+12}$ mm	57 mm

Table 5. ECAL end-cap tertiary (L1) 240-fiber fan-out specifications

Fan-out Type	Total fiber length	Ferrule length
L1-1B-A	1530 $^{-0}/_{+20}$ mm	100 mm
L1-1B-B	940 $^{-0}/_{+10}$ mm	100 mm

The large number of ferrules required for the tertiary distribution system and the technical problems (e.g. split cladding) posed by polishing silica-polymer fibers bonded in relatively soft polyetherimide ferrules lead the manufacturer, SEDI [18], to propose a more cost effective solution using controlled cleavage rather than cutting and polishing. This technique is used extensively in the communications industry on smaller diameter fibers, leaving an unfinished cleaved face at the ferrule end. The manufacturer adapted the method to the 200 μm silica core fibers used in this application by developing a special ferrule bonding technique: in a first step, each fiber is glued [17] into its ferrule assembly (at a fixed distance from end), and cured at room temperature. Then the excess of each fiber is cleaved using a SpectTran CT-2 mechanical cleaver. The cleaved face retracts into the ferrule several microns. Transmission and aging tests in the final geometry performed showed results equivalent to polishing, with improved production uniformity.

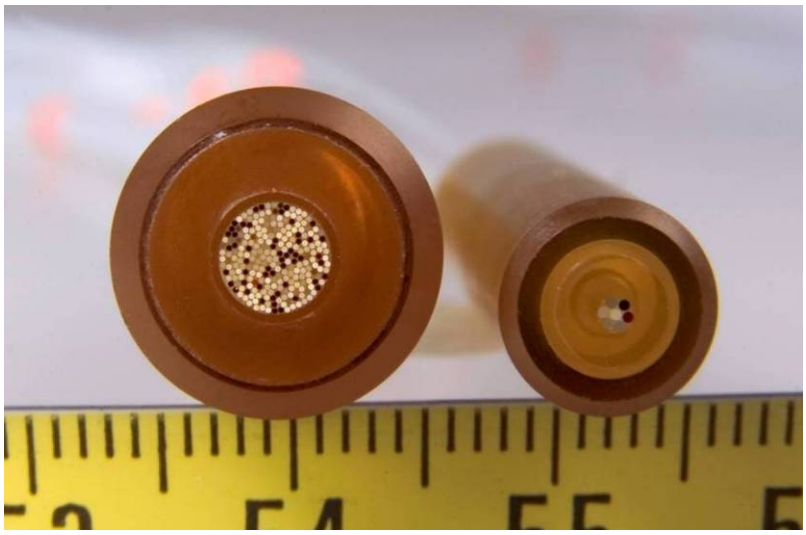

Figure 12. *Polished fiber-bundle tube faces (fibers are bonded into the insert, outer ring is bundle tube): at left, 240-fiber barrel Tertiary (L1) fan-out and at right, 7-fiber Secondary (L2) fan-out. Dark fibers in the photo have color-coded protection caps to indicate that they have been selected or rejected.*

The fan-out assembly is completed when fibers are stripped 5 mm (sheath removed 20 mm) and glued [17] into the fan-out's fiber-bundle tube assembly shown in Fig.12. The bundle tube is assembled following the same procedure as for the secondary fan-out discussed previously: a 10 mm long molded Ultem® centering insert holding the fibers is glued into a 70mm long extruded Ultem® tube of the appropriate diameter depending upon the fibers which are used: 12mm O.D. for the barrel and 14mm O.D. for the end-caps. A positioning collar 1.9 mm long on the centering insert ensures its mechanical positioning in the diffusing

sphere. Again the diameters are different for the barrel (4.6 mm O.D.) and end-cap (4.8 mm O.D.) applications. The cured fan-out is polished on the bundle tube face. Tests showed that the fiber bonding withstands tractions > 2 daN.

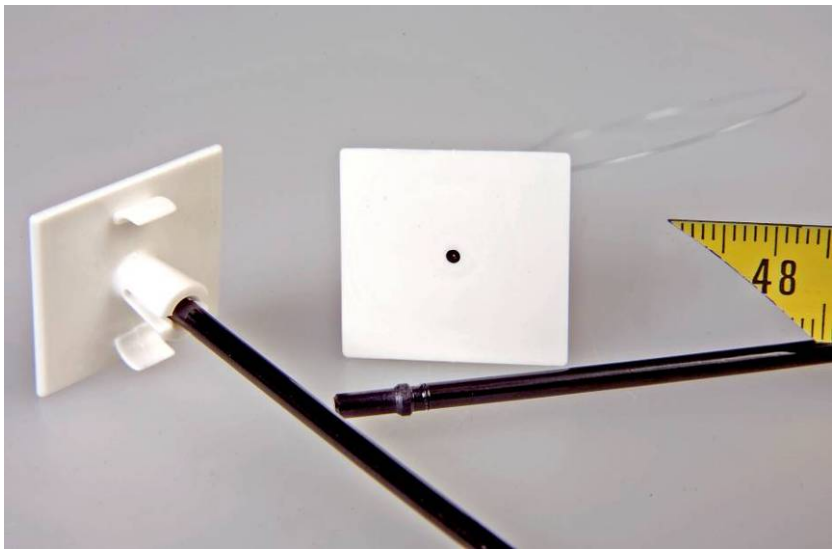

Figure 13. *An ECAL barrel ferrule support, showing the fiber ferrule snapped in place.*

2.4.4. Crystal ferrule support.

Molded ferrule supports are used to position each tertiary fiber with a well-defined 300 ± 25 μm air gap between the fiber end and the $PbWO_4$ crystal. This method avoids potential transparency losses due to radiation damage or aging from epoxy or glue. Barium sulfate loaded polycarbonate is used for efficient light diffusion. A snap-lock on the support captures a ring molded on the ferrule to fix the fiber's position. Since the light injection into the crystal differs, as outlined in the overview (sect. 2.1), between the ECAL barrel and ECAL end-cap designs, two different ferrule supports are used. The ferrule support used in the barrel application is shown in Fig. 13. These supports are designed to fit into the bottom of the alveola holding the crystal, as shown in Fig. 14. Altogether 6 ferrule support types are required to adapt to the different crystal dimensions in the barrel (varying with η), ranging from type 1 (21.8 x 22.3 mm) to type 6 (21.8 x 24.1 mm). In the end-cap application shown in Fig. 15, the tertiary (L1) optical fiber's 100 mm long ferrule passes through an access hole machined in a corner of the aluminum insert housing the VPT and is snapped into a molded ferrule support held in the insert at the rear face of the crystal. Since all end-cap SC use the same size crystals, only a single support type is required.

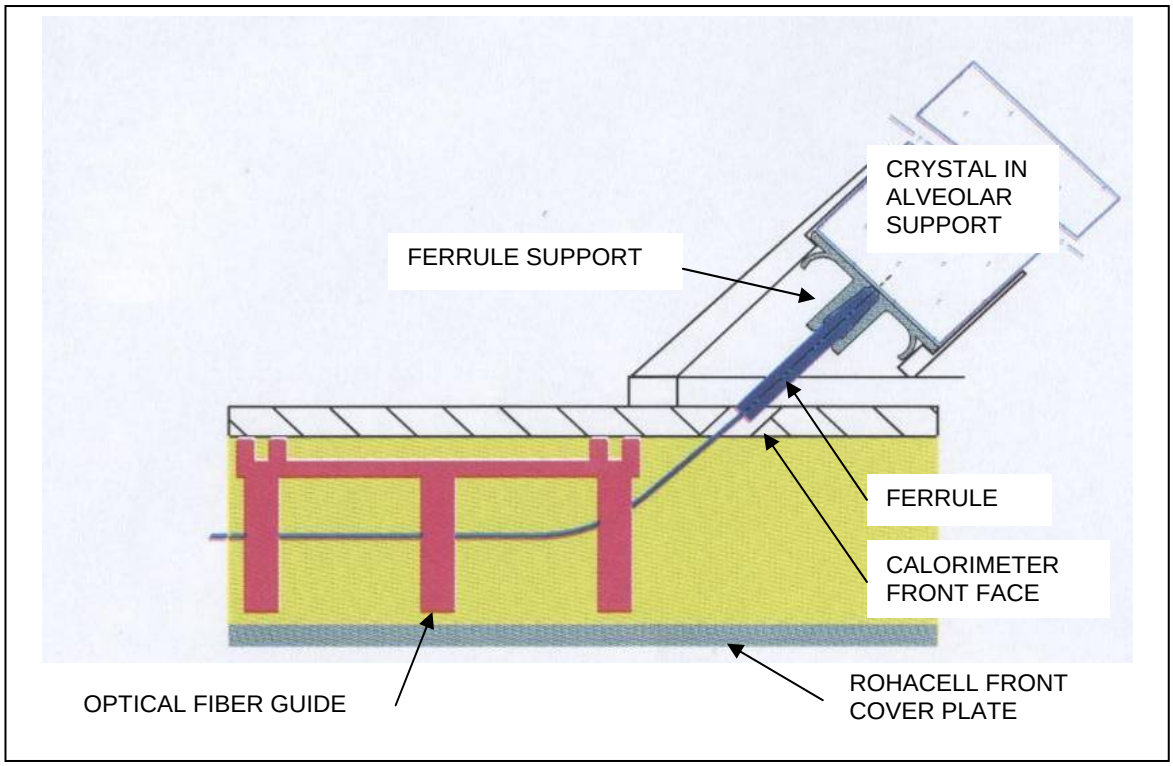

Figure 14. *Light distribution for the barrel crystals, showing the light injection via the crystal's front-face (LHC interaction point is below and to the left).*

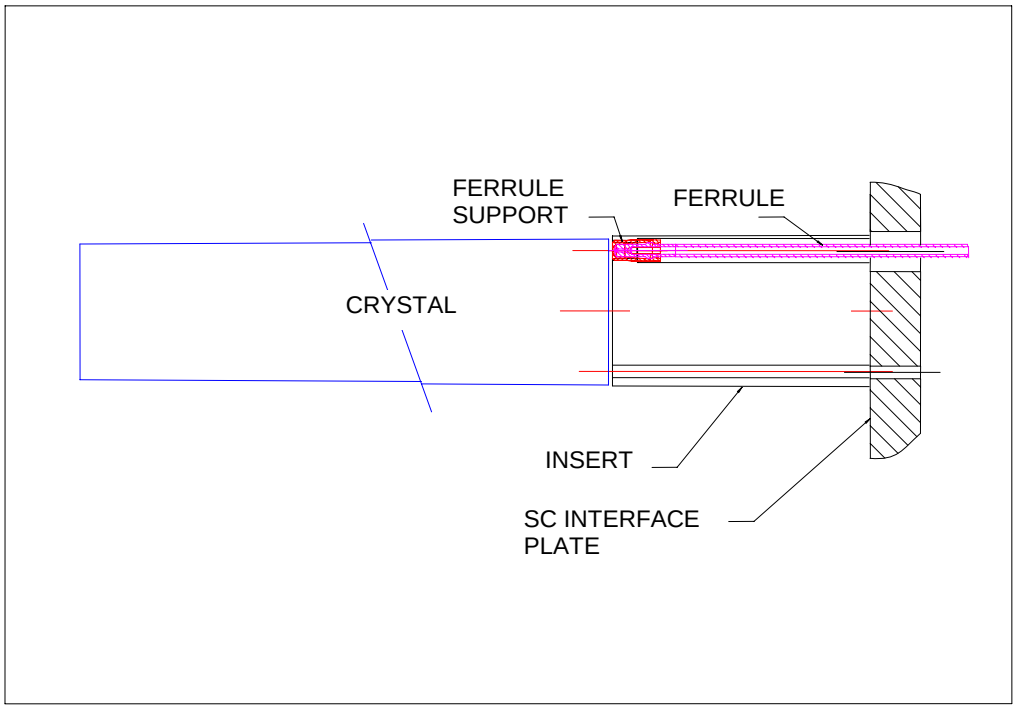

Figure 15. *Light distribution for the end-cap crystals, showing the light injection via the crystal's rear face (LHC interaction point is to the left).*

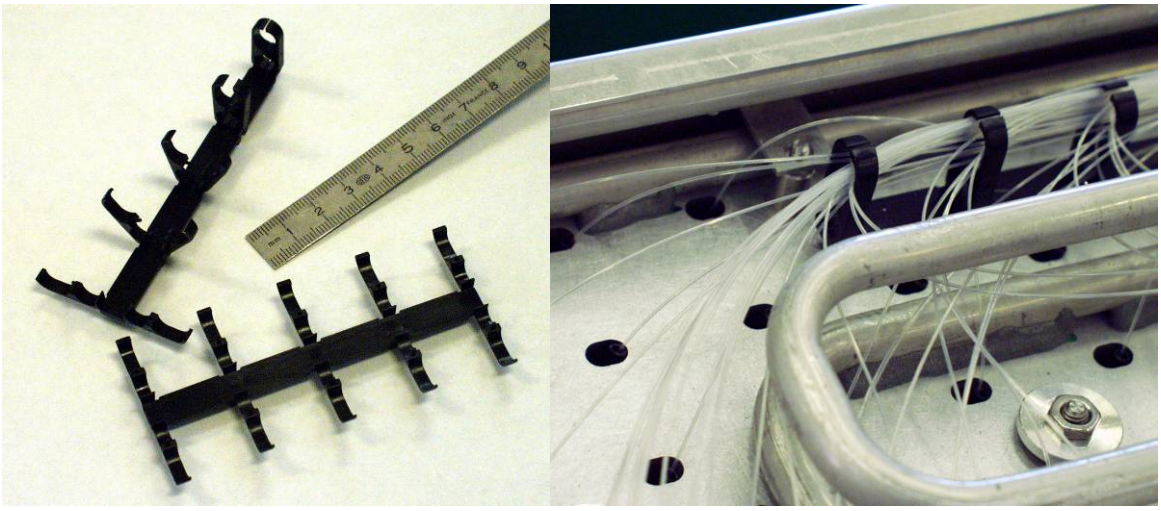

Figure 16. *Molded optical-fiber guides with a snap-lock feature are shown in (a). In (b) the guide is installed on the SM front face near the cooling tubes.*

2.4.5. Fiber guides and neutron moderator.

Molded polycarbonate optical-fiber guides with a snap-lock feature are glued (acrylic) on the SM front-face to simplify the installation of the tertiary fibers. This is particularly useful in the delicate region near the cooling tubes.

In order to reduce the neutron flux in the CMS central silicon tracker, a neutron moderator consisting of molded polyethylene grains (roughly 3 mm diameter) with a density of 0.95 g/cm^3 is used to fill the entire free volume between the calorimeter cover and the front face occupied by the monitoring system components. This solution adds moderator, without increasing the radial thickness of the calorimeter. A series of test fillings on a prototype were performed to determine that the mean packing fraction of the available volume is 62 ± 2%. In reality, 13 kg of moderator are used per SM (accounting for cooling tubing, optical fiber distribution system, FEM units, etc.), yielding an average of 1.11 g/cm^2 of polyethylene, equivalent to a mean thickness of 1.17 cm. The use of grains simplifies any eventual interventions as the moderator can be easily removed with a vacuum cleaner without damaging the installed fibers.

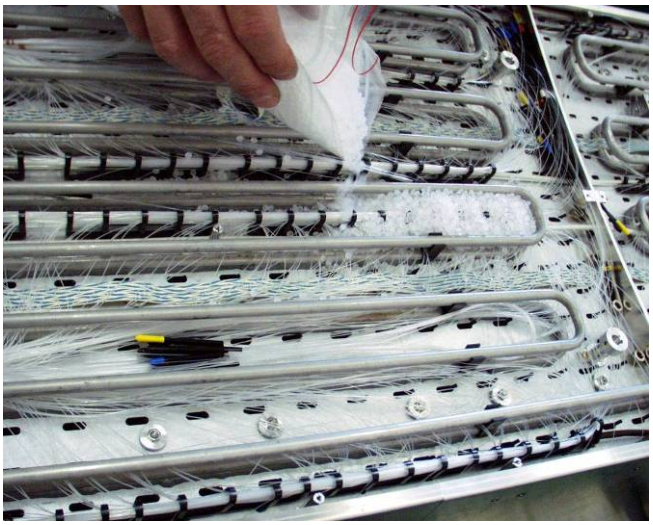

Figure 17. *Molded polyethylene grains, used as a neutron moderator, are filled into the region occupied by the monitoring system before the front cover of the SM is mounted.*

2.5. Reference PN photodiodes

As outlined in the system overview, the relative calibration of injected laser light on each group of crystals is achieved by injecting the light simultaneously via the tertiary optical fiber distribution on to pairs of reference PN photodiodes mounted on the calorimeter element. These reference photodiodes must be stable, radiation hard and insensitive to the magnetic field (4 Tesla). PN type photodiodes were chosen for this role due to their very narrow depletion zone (~7 μm with +4 V reverse bias), making them much less sensitive to type inversion than the faster PIN photodiodes. These photodiodes operate with unity gain, thereby giving reliable stability independent of bias voltage and temperature. The typical device capacitance is ~80 pF. A series of radiation studies were performed to select an appropriate photodiode, yielding the final decision to use the Hamamatsu PNN+ type 1227-33BQ silicon photodiode with a quartz window. Optimum long term stability, signal/noise ratio and radiation hardness are obtained with a shaping of 1 μs and a reverse bias of +4 V; the shaping is well adapted to the ~100 Hz pulse rate of the laser source. As a result the reference photodiode system gives reproducible, essentially linear, responses to variations of laser pulse energy, which are nearly insensitive to laser pulse width variations (the performance implications of this issue will be addressed in section 5.3). Performance of the PN photodiodes under irradiation is discussed is sect. 3.4.1.

Altogether, 528 PN photodiodes are used on the ECAL. They are mounted in front-end units described below. Each front-end unit serves a pair of secondary (L2) or tertiary (L1) optical fiber fan-outs. Since only one line of fan-outs is pulsed by the laser at a time (recall that a calorimeter element is a half-SM for the barrel), we have added redundancy against component failure without increasing the number of PN photodiodes by distributing two fibers to each PN photodiode (one from each fan-out, see for example Fig. 5). In this way both PN photodiodes independently measure the laser pulse sent to the fan-out. This is achieved by mounting the respective pair of optical fibers into a single ferrule (glued, cut, and polished together).

All of the production reference PN photodiodes came from one of two production wafers. A sub-sample of 10 units was tested before accepting delivery to ensure that: a) the dark current is < 30 pA, and b) that the quantum efficiency is $\geq 64\%$ at 450 nm and 532 nm, and $\geq 63\%$ at 660 nm. Once mounted, all were tested and characterized along with their associated electronics after assembly of the front-end units; the procedure and results are discussed in sect. 4.3.

2.6. PN photodiode read-out electronics

2.6.1. Front-end ASIC charge sensitive preamplifier.

Each pair of reference PN photodiodes is read out locally on the calorimeter using a dedicated radiation-hard ASIC twin channel front-end chip designed in 0.8 μm CMOS DMILL technology. The PN diodes are coupled capacitively to the ASIC via 100 nF ceramic capacitors. Each channel, shown in Fig. 18, consists of a remotely switched dual-gain low noise charge amplifier designed to match the photodiode's capacitance, a 1.16 μs type single-integration single-differentiation RC shaper, and a 50 Ω output buffer. The switchable gain allows the ASIC to cover two dynamic ranges: a) gain A covers laser pulses up to an equivalent maximum energy deposit of 120 GeV, and b) gain B covers the range up to 2 TeV, where it should be noted that the deposited energy of an electron in a single crystal is

typically 75% of its incident energy. Dynamical characteristics for both gains are summarized in Table 6. The rather long shaping time was chosen to optimize the S/N ratio. The chip design, shown in Fig. 19, separates the two channels to reduce cross-talk, and isolates the charge sensitive preamplifiers from their respective shapers and output buffers. Only the calibration injection voltage V_{inj} and slow control circuits are common to both channels. Power consumption is 50 mW per channel.

The internal calibration circuit included in the ASIC is used to inject a well defined charge into each input. This charge is generated locally in order to avoid introducing noise in nearby electronics. The circuit is designed to be stable and sufficiently radiation-hardened to ensure 0.1% inter-calibration over 10 years of LHC operation. This is achieved by applying an externally driven calibrated injection voltage (V_{inj}) from 0 to 5V (limited by DMILL specifications) to a measured internal capacitor (C_{inj}), typically 2.0 pF, via switching transistors which are also integrated into the ASIC. The value of C_{inj} is measured for each channel during ASIC characterization (see section 4.2). Typical transistor switching time is 2 ns.

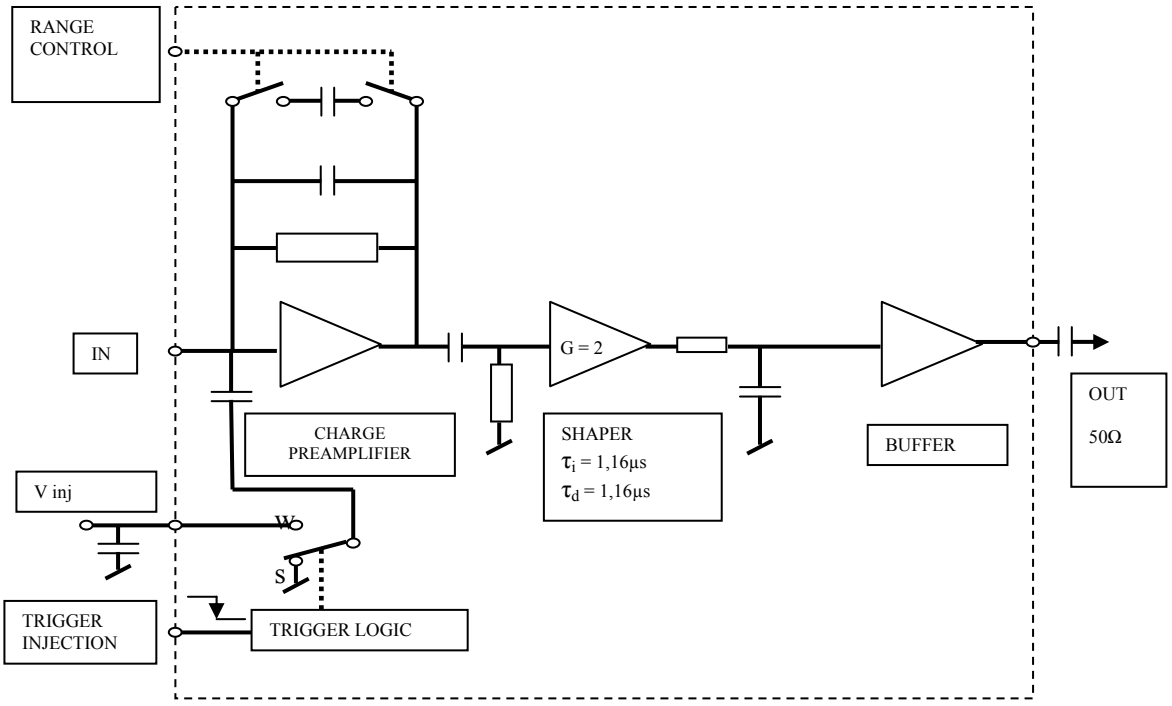

Figure18. *Schematic diagram of the ASIC front-end circuit (a single channel is shown here).*

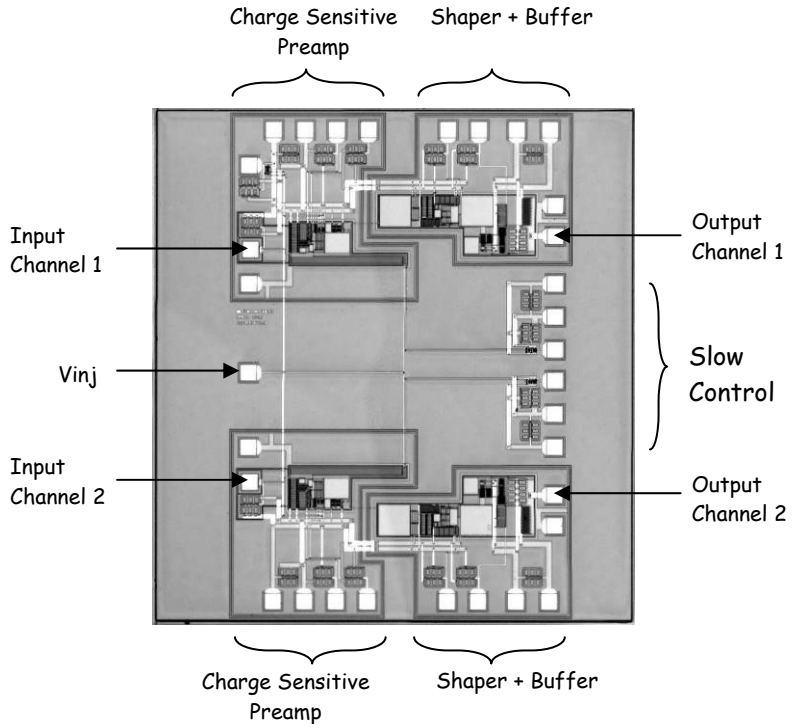

Figure 19. *Photomicrograph of the twin front-end ASIC designed for the PN photodiodes. The separated "twin" structure (top and bottom) is clearly visible, as is the isolation of the individual channel's low noise preamplifier.*

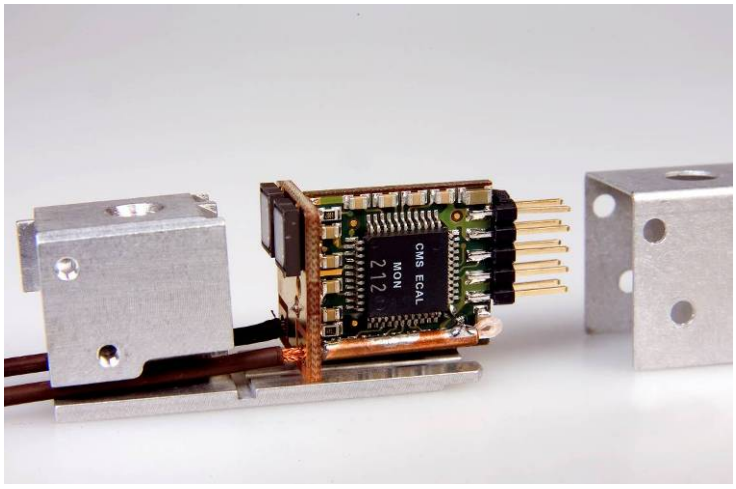

Figure 20. *The FEM unit: at left is an aluminum block used to position the optical fibers, at the center, is a T-shaped circuit-board containing the two PN photodiodes (left-side) and the twin-channel Front-end ASIC. A bus-line (pins to the right) carries the bias voltage and control lines.*

The front-end ASIC is mounted along with the pair of PN photodiodes in a FEM (Front-End Module) assembly, shown in Fig. 20. The dimensions of the FEM are constrained by the 22 mm height available to install the monitoring system in the ECAL barrel design. The mechanical assembly consists of three parts: 1) a machined aluminum block into which the optical-fiber ferrules are rigidly positioned 300 ± 25 μm in front of the PN photodiodes, 2) a T-shaped circuit board onto which the two Hamamatsu 1227-33BQ silicon photodiodes are mounted orthogonally to the twin-channel ASIC, and 3) an external cover for shielding. The individual photodiode's 5.7 mm^2 sensitive area guarantees sufficient tolerance in the

alignment of the input ferrule. Analog signals from the front-end chip are sent via 50 Ω coax cables (barrel: 3 m, end-caps: 7 m) to the MEM module. A flat twisted-pair bus-line carries the bias voltage and slow control lines.

Table 6. Dynamical range of the Front-end CMOS DMILL ASIC twin-channel preamplifier. *Values given are typical values for a C_{inj} of 2.0 pF. The equivalent deposited energy of an electron centered on a crystal is typically 75% of its incident energy. The full range of gain B is not exploitable with a calibration test pulse V_{inj} (DMILL ≤ 5V maximum).*

GAIN A	**σ noise (system)**	**Maximum**
Equivalent Deposited Energy (GeV)	$90 \cdot 10^{-3}$	120
Charge at input (pC)	$0.9 \cdot 10^{-3}$	1.0
Charge at input (e^-)	5600	$7.5 \cdot 10^6$
Equivalent V_{inj} (mV)	0.45	600
V_{out} on 50 Ω (mV)	0.4	500
GAIN B	**σ noise (system)**	**Maximum**
Equivalent Deposited Energy (GeV)	0.51	2000
Charge at input (pC)	$5.0 \cdot 10^{-3}$	17
Charge at input (e^-)	32 000	$130 \cdot 10^6$
Equivalent V_{inj} (mV)	2.6	Out of DMILL specifications
V_{out} on 50 Ω (mV)	0.12	1000

2.6.2. MEM 10-channel onboard digitizer module.

Analog signals from10 front-end channels, 5 FEM units, are digitized in a MEM (Monitoring Electronics read-out Module) mounted at the extremity of the SM (barrel) or in the cabling duct outside the Dee (end-caps). The MEM layout is composed of two nearly independent halves, each treating 5 channels. The system robustness is strengthened by treating separately the even and odd channels of each FEM. The design is shown schematically in Fig. 21, where the first 5 channels are labeled PN1+ and the second 5 channels are labeled PN1-. In the first level of data treatment, the signals are digitized in parallel using 10 Analog Devices AD9042 monolithic 12 bit 40 MHz analog-to-digital converters (ADC), coupled to CRT245 radiation hard output buffers. In the next level, two ECAL Front-End (FE) read-out boards [20] are used to read-out the data. Originally designed for a 25-channel calorimeter tower with a nominal frame length of 10 time samples, the FE board contains 5 strip-FENIX chips (multipurpose DAQ and Trigger task chip in 0.25 μm IBM technology). In order to adapt to the slower PN signals in the MEM application, the 5 ADC channels served by the FE board are multiplexed to the inputs of each of the 5 strip-FENIX chips. The time frame is then simply enlarged by sequentially shifting each strip-FENIX chip by 10 time samples with respect to the precedent.
The use of two standard FE read-out boards means that the MEM is seen by the CMS readout system as two additional ECAL trigger towers. As for other ECAL channels, data is transferred from each FE board via optical fiber; the task is assured by a 16-bit serialized laser driver Gigabit-optical-hybrid (GOH) mounted on a mezzanine circuit board. Furthermore, as for the rest of the ECAL FE read-out, the MEM is controlled and clocked by two redundant token rings which address the two Front-End boards using I2C protocol via a Communication and Control Unit ASIC (CCU, designed in 0.25 μm IBM technology) mounted on the FE circuit board.

In addition to digitization of PN photodiode signals, the MEM supplies service, control and V_{inj} level for charge injection to the FEM units via a bus-line. The FEM injection trigger as well as the even and odd channel gains are defined by 5 V level transitions which are obtained from the respective FENIX 2.5 V levels using pair complementary NPN-PNP transistors (HFA3134-HFA3135) built using Intersil UHF-1X technology. Two Detector Control Unit ASICs (DCU) designed in 0.25 µm technology, are mounted on the motherboard, one for each Front-End board. The DCU has an internal 12-bit ADC (0.25 µs conversion time) with 6 multiplexed inputs, and is designed for voltage, current and temperature measurements. In the MEM design five of the inputs are used: channel 0: unused, channel 1: motherboard temperature, channel 2: (1/2) V_{DD1}, channel 3: (1/5) V_{inj}, channel 4: (1/2) V_{DD2}, and channel 5: (1/5) V_{CC}, where V_{DD1} and V_{DD2} are digital voltages (2.5 V) and V_{CC} is the analog voltage (5 V) used for both the FEMs and ADCs.

Altogether 35 watts of heat are produced by the MEM. This is extracted by using a water-cooled aluminum plate (shown in Fig. 22). Thermal contact between the plate and the various sources of heat is obtained by using silicon gel thermal pads between the electronics components and the plate itself, or via an intermediate cooling bar as in the case of the ADC chips (at the entry) or the power regulators (at the rear of the motherboard). Two types of thermal pads are used: 1) for the ADC and thermal regulators: Dow Corning TP-2100 alumina-filled silicon gel thermal pad, 2.2 mm thick (0.7 Watt/m-°K), and 2) for the FENIX, GOH ASICs and beneath the motherboard: Bergquist Company "Gap Pad" (GPVOUS-0.040-AC-816-NA). The resulting temperature stability is largely sufficient for the specifications of the AD9042 digitizing chip: the offset stability is ≤ 25 ppm/°C and the gain stability is ≤ |-50| ppm/°C.

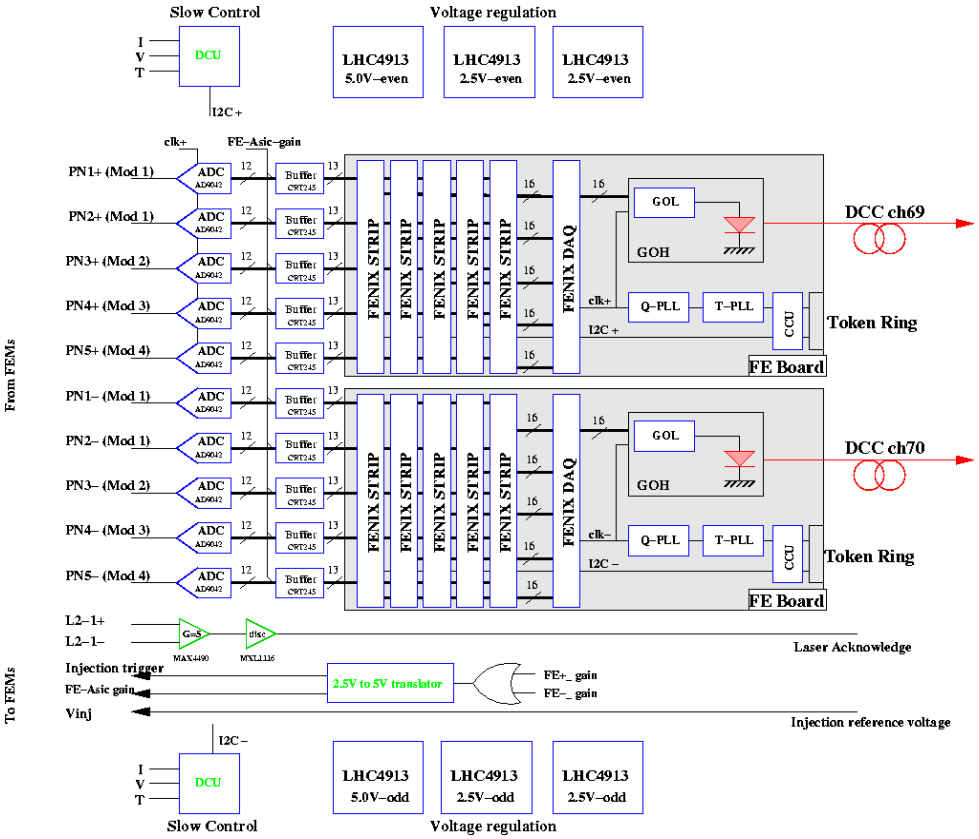

Figure 21. *Schematic diagram of the MEM 10-channel digitization module. Two 5-channel ECAL FE boards are used to read-out the line of 10 ADCs. Their outputs are sent to an ECAL Data Concentrator Card (DCC).*

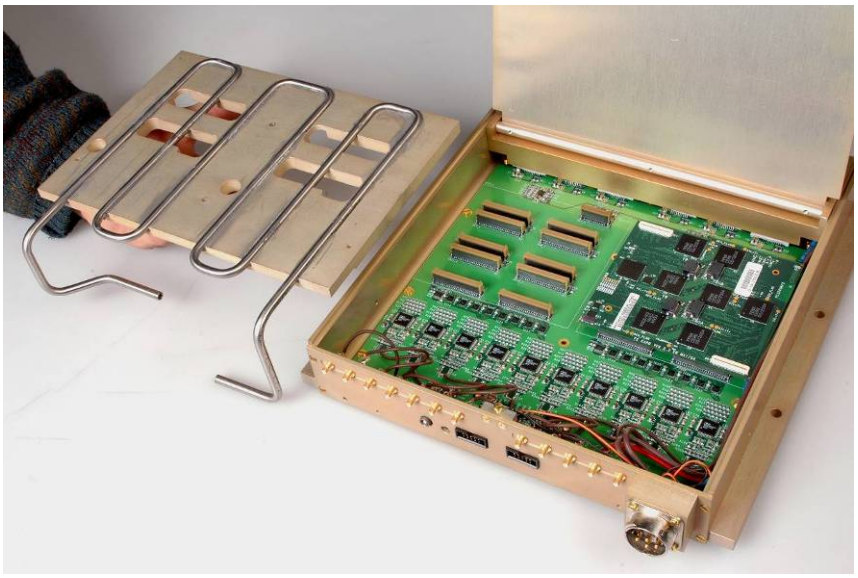

Figure 22. *The MEM 10-channel digitizer module with its water-cooling plate (at left) removed: the 10 ADCs serving each of the input channels can be seen at the bottom, and at the top are the two ECAL Front-End boards (one removed here).*

3. Monitoring system component radiation hardness evaluation

3.1. Radiation tests

All components of the monitoring system which risk exposure to irradiation were tested individually or, if more appropriate, as a subsystem at one or more of the following facilities: 1) ULYSSE 100 kW reactor, INSTN CEA-Saclay, France, 2) COCASE (Co^{60} gamma ray source), CEA-Saclay, France, or 3) 63 MeV proton beam at the Paul Scherrer Institute (PSI), Villigen, Switzerland. In the case of the irradiations at the ULYSSE reactor, it should be clear that components were simultaneously exposed to fission spectrum neutrons, thermal neurons and gamma-rays.

The system requirements depend upon where the components are situated in CMS. The potentially sensitive items are the optical distribution elements and FEM units located at the front of the ECAL barrel, and the same elements located behind the ECAL end-cap crystals (FEM at radii $\geq$ 1300 mm). Only the ECAL barrel MEM units are located within the exposed region. The Table 7 below summarizes the maximum exposure expected in each region assuming a 10 year LHC integrated luminosity of $5 \cdot 10^5$ pb^{-1}[11].

Table 7. Expected component exposure for an LHC integrated luminosity of $5 \cdot 10^5$ pb^{-1}.

Region components installed	Maximum total neutron fluence	Maximum Total dose
ECAL BARREL: front face	$3 \cdot 10^{13}$ n/cm^2	3 kGy
ECAL BARREL: MEM position	$2 \cdot 10^{13}$ n/cm^2	0.3 kGy
ECAL END-CAPS: behind crystals	$1.5 \cdot 10^{14}$ n/cm^2	20 kGy
ECAL END-CAPS: FEM r $\geq$ 1300 mm	$3 \cdot 10^{13}$ n/cm^2	4 kGy

Optical and passive components were studied in a series of 4 runs in 1999 at the ULYSSE reactor: January: $5 \cdot 10^{12}$ n/cm^2, May: $1.5 \cdot 10^{13}$ n/cm^2, June: $1.5 \cdot 10^{14}$ n/cm^2, and December: $3.5 \cdot 10^{14}$ n/cm^2. Table 8 below summarizes the various components and the respective total

neutron fluence and total dose received. Optical tests were performed on elements such as optical fiber, diffusing sphere, or secondary (L2) light guide; with the exception of the optical fibers discussed below, the results after irradiation agreed within errors with those obtained prior to exposure. Concerning the passive components, no visual changes were noted, except a slight yellowing of the polycarbonate ferrule support at $3.5 \cdot 10^{14}$ n/cm^2. No deterioration of mechanical properties was observed.

Table 8. Irradiation tests of optical & passive components at ULYSEE reactor, Saclay

Component	Material	Total fluence	Dose
Optical fiber (HCG MO365T)	Silica-silica-polymer-Tefzel®	$1.5 \cdot 10^{14}$ n/cm^2	6 kGy
Optical fiber (HCP MO200T)	Silica-polymer-Tefzel®	$1.5 \cdot 10^{14}$ n/cm^2	6 kGy
Diffusing sphere (Spectralon®)	Thermoplastic resin	$3.5 \cdot 10^{14}$ n/cm^2	13 kGy
L2 aluminization	Aluminum + SiO_2	$1.5 \cdot 10^{13}$ n/cm^2	0.6 kGy
ST connector	Arcap & polymer	$1.5 \cdot 10^{14}$ n/cm^2	6 kGy
Vpin connector (Ultem®)	polyetherimide	$3.5 \cdot 10^{14}$ n/cm^2	13 kGy
Fiber bundle tube (Ultem®)	polyetherimide	$3.5 \cdot 10^{14}$ n/cm^2	13 kGy
Epoxy [17]	Epoxy resin	$1.5 \cdot 10^{14}$ n/cm^2	6 kGy
Ferrule support	polycarbonate	$3.5 \cdot 10^{14}$ n/cm^2	13 kGy
Mechanical glue	Acrylic	$1.5 \cdot 10^{14}$ n/cm^2	6 kGy
Rigid foam	polymethacrylimide	$1.5 \cdot 10^{14}$ n/cm^2	6 kGy
Cover	fiberglass	$1.5 \cdot 10^{14}$ n/cm^2	6 kGy
Neutron moderator	polyethylene	$5 \cdot 10^{12}$ n/cm^2	0.2 kGy
Dow Corning thermal pad	Alumina filled silicone gel	$2 \cdot 10^{14}$ n/cm^2	8 kGy

3.2. Thermal pad conductivity stability under irradiation.

In addition to mechanical properties, measurements were made of the relative thermal conductivity (before and after irradiation in the ULYSEE reactor) of the Dow Corning GTQ2100 silicone gel pad used to transfer heat from the MEM module components to the cooling system. An assembly of 9 series thermal junctions each 25 x 25 mm^2 x 1.8 mm thick was arranged such that each junction received the same neutron fluence and dose. The conductivity was determined by placing the assembly between a 12.5 W thermal source and an aluminum heat sink at constant temperature; following the evolution of the temperature with time using PT100 probes. These measurements were performed prior to irradiation and three weeks after exposure to a fluence of $2 \cdot 10^{14}$ n/cm^2 neutrons. The relative conductivity was determined from the differences in the slopes of the dynamic transfer $\Delta T/\Delta t$ from 30 sec to 10 minutes. An increase in the thermal conductivity of $7.9 \pm 0.2\%$ is observed after irradiation. Clamping was unchanged throughout tests.

3.3. Optical fiber transmission loss measurements after irradiation.

A number of studies of radiation damage in optical fibers have been reported, most of these concern infrared wavelengths used in optical link communication [21]. Few measurements at optical wavelengths were available, and these had often been taken during irradiation at reactors, or cyclotrons where the flux was well above LHC conditions [22]. Since radiation damage in silica-core optical fibers is primarily due to creation (and/or activation) by ionization of absorption centers called “color centers”, which can subsequently recover (and/or deactivate) by various mechanisms such as thermal annealing, absorption during irradiation depends upon the relative dynamics of the two competing processes. Measurements much closer to our expected situation at LHC are those of residual induced

absorption loss taken at equilibrium following irradiation. A series of irradiations were undertaken to study this condition. In order to obtain sufficient precision for the optical fiber transmission losses, 200 m long rolls were tested in a first series of irradiations up to a fluence of $1.3 \cdot 10^{13}$ n/cm^2 and 50 m long rolls were used in a second series of irradiations up to $1.5 \cdot 10^{14}$ n/cm^2. The transmission at 6 different wavelengths (412, 441, 527, 582, 602 and 633 nm) was measured before, during and after exposure. The results are described using the usual expression for attenuation in an optical fiber written as the sum of the initial and induced attenuations

$$A(\lambda) = A_0(\lambda) - 10/L \cdot \log_{10}(I_{irr}(\lambda)/I_0(\lambda))$$

where $A_0(\lambda)$ is the attenuation before irradiation, L is the fiber length, and $I_0(\lambda)$ and $I_{irr}(\lambda)$ are the transmitted light intensities before and after irradiation. The typical initial attenuation at 440 nm for fibers used for the light distribution system is 0.025 db/m for the SpecTran silica-polymer core fibers used on the ECAL barrel tertiary fan-outs or 0.018 db/m for the SpecTran silica-silica core fibers used for the ECAL end-caps tertiary fan-outs (as well as all of the secondary fan-outs). Typical reactor exposures lasted 2 hours. The results for the optical fibers showed a rapid increase of absorption during irradiation and a rapid recovery (time constant of 3 to 7 hours) after irradiation, reaching a value of residual induced attenuation superior to the initial value several weeks later. Subsequent irradiations indicate that the absorption during irradiation rapidly regains the previous level, finally increasing with total fluence, and that recovery after irradiation shows accumulative induced attenuation. This argues for deactivation and not permanent recovery of produced color centers on the time scales studied. The residual induced attenuation at 440 nm observed at a total integrated neutron fluence of $1.5 \cdot 10^{14}$ n/cm^2 (dose of 6 kGy) is 0.15 ± 0.02 db/m for the silica-polymer fiber, and 0.04 ± 0.02 db/m for the higher OH^- ion content silica-silica fibers. Considering the short maximum lengths of optical fibers exposed in the system (ref. Tables 3, 4 and 5), these results are well below 1% induced attenuation loss/year for the optical distribution system at LHC (10^{34} cm^{-2} s^{-1}).

3.4. Irradiation tests of electronics components.

Studies to evaluate the performance of the PN photodiodes and their associated read-out electronics are summarized in Table 9.

Table 9. Irradiation tests of monitoring system electronics components

Component	Total fluence	Dose	Irradiation Facility
Hamamatsu 1227-33BQ PN silicon photodiode	$5 \cdot 10^{13}$ n/cm^2	2 kGy	ULYSSE reactor, Saclay
Front-end DMILL ASIC	$1.5 \cdot 10^{14}$ n/cm^2	6 kGy	ULYSSE reactor, Saclay
MEM	$1.5 \cdot 10^{13}$ p/cm^2 @ 63 MeV	20.5 kGy	Paul Scherrer Institute (PSI), Villigen

3.4.1. PN Photodiode quantum efficiency stability under irradiation.

A key aspect to the performance of the laser monitoring system at LHC is the stability of the reference PN photodiode quantum efficiency under irradiation. Quantum efficiency measurements performed on a series of 10 photodiodes subjected at the ULYSSE reactor to a total neutron fluence of $5x10^{13}$ n/cm^2 and a total dose of 2 kGy gave a mean quantum efficiency loss of 0.7% at 470 nm (blue) and 0.4% loss at 532 nm (green), well within the

design requirements of the system. The drop of quantum efficiency loss with increasing wavelength is consistent with what is expected if the main source of damage is due to γ irradiation inducing a positive charge density at the interface between the passivation layer and the silicon; deeper conversion of longer wavelength photons would be less sensitive to any electrical field inversions near the surface. However, this trend was not confirmed by measurements at 675 nm (red) which gave a mean quantum efficiency loss of 10%, with a comparable spread; we suspect in this case that charge carriers in the weak field zone may be affected by bulk defects created by the neutron fluence. Nevertheless, one should keep in perspective that the loss in red is accumulated over an irradiation equivalent to 10 years of running at LHC, and therefore does not jeopardize short-term transmission stability measurements using the red laser. The mean dark current I_D following this irradiation was 18 nA, where $I_D < 30$ pA for a non-irradiated PN (see sect. 2.5).

3.4.2. Front-end ASIC performance after irradiation.

The performance of a sample of 10 front-end ASICs (powered during exposure) measured two weeks after irradiation at the ULYSSE reactor confirmed the performance of radiation-hard DMILL technology: after a fluence of 10^{14} n/cm^2 gain loss was typically ≤ 3%, and both rise time and noise increased by ≤ 7%. Cross-talk between channels remained unchanged. Since gain changes are corrected using the calibration circuit, these results are within our specifications.

3.4.3. MEM functional tests during and following irradiation.

Most of the individual components used to build the MEM have been radiation tested previously [23]. The objective of the irradiation tests at PSI was to validate the assembled system. A pre-series MEM board was mounted in the 63 MeV proton beam line. The incident intensity was $1.25 \cdot 10^9$ p/cm^2/s, defocused such that it covered half of the MEM board (a surface of 10 x 10 cm^2 containing one full FE board). The exposure lasted 3 h 20 min, yielding an equivalent total ionizing dose of 20.5 kGy. Failure of the token ring during the very high dose rate made it impossible to test functionality during irradiation. Nevertheless, full recovery was observed in tests 24 hours after irradiation.

4. Monitoring system characterization & installation

Characterization of monitoring system components was essential to control the quality of the production. Since the physics objective of the system is the channel-to-channel measurement of deviations in the crystal transparency terms and not their absolute values, individual channel characterizations, such as optical fiber transmission, are not required for the analysis data base. However, systematic effects are reduced if the spread of the response of the assembled system is not large; this aspect introduced the selection cuts in the characterization measurements described below.

4.1. Optical fan-out validation and characterization.

All optical fan-outs were pre-tested at the factory and compared against a reference fan-out using a stable light source, an integrating sphere and a photodetector (precision ± 0.1 dB). Fibers were accepted if the relative loss was ≤ 0.45 dB; bad fibers were marked and a tertiary L1 fan-out was accepted if ≤ 30 out of 240 fibers were rejected. The manufacturer was allowed to replace up to 20 “bad” ferrules, under the condition that the fiber length remained within 70 mm of the specified length. Fan-outs passing these preliminary specifications were delivered to Saclay. After delivery all fan-out were burned-in to remove defects prior to

transmission measurements: two 72 hour cycles in an oven at 75° C were separated by 24 hours at room temperature. This procedure was adopted after prototype studies revealed 5 to 10% transmission losses for ~3% of the channels of fan-outs stored for a period of several months at room temperature. Following the series of ageing cycles, each fan-out's transmission was measured on a robotized bench. The bench, shown in Fig. 23, used a 632 nm (red) helium-neon laser coupled via 10 m of optical fiber to a Spectralon® [19] integrating sphere (see section 2.4.3) into which the fan-out to be tested was inserted. A reference PN photodiode was also connected to the integrating sphere. The individual fibers were inserted into a 16x16 array of ferrule supports mounted in a machined plate. They were scanned by a second PN photodiode positioned by two computer controlled stepping-motors via CAMAC. The currents produced by the two PN photodiodes were read-out with picoammeters connected to the computer via a GPIB bus-line. The data was recorded using Labview.

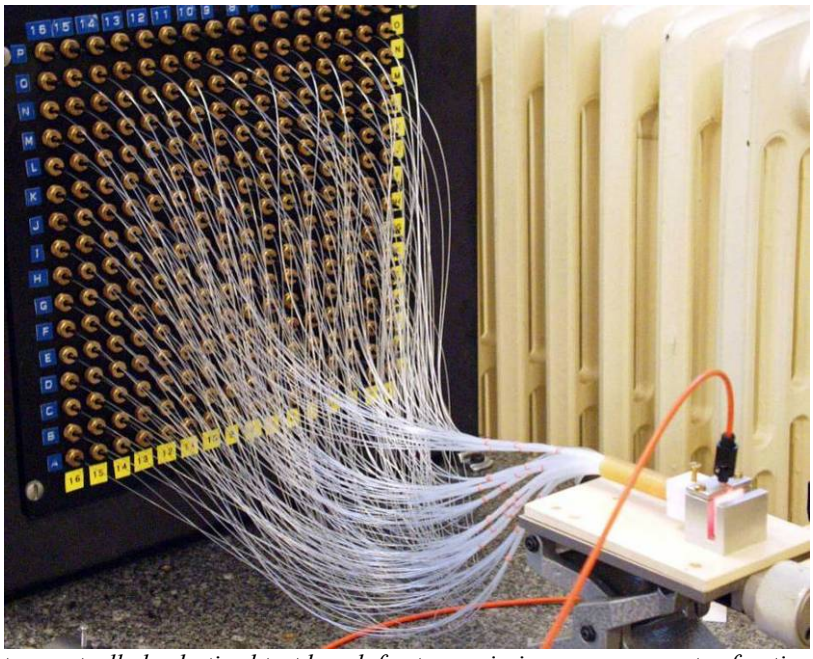

Figure 23. *Computer controlled robotized test bench for transmission measurements of optical fiber fan-outs.*

Typical results of transmission measurements are shown in Fig. 24 for the 9 tertiary (L1) fan-outs of a SM. Measurements of tertiary fan-outs yield a spread of 2.4% RMS in their individual mean transmission values. Fibers are selected by averaging three measurements and normalizing the results for each fan-out; fibers are selected if within ± 7% of the mean. Typically 97% of the fibers are within these specifications; fan-outs with less than 210 selected fibers are rejected and returned to the fabricant for repair/replacement. The 10 fibers nearest the mean value are marked for eventual use with the reference PN photodiodes.

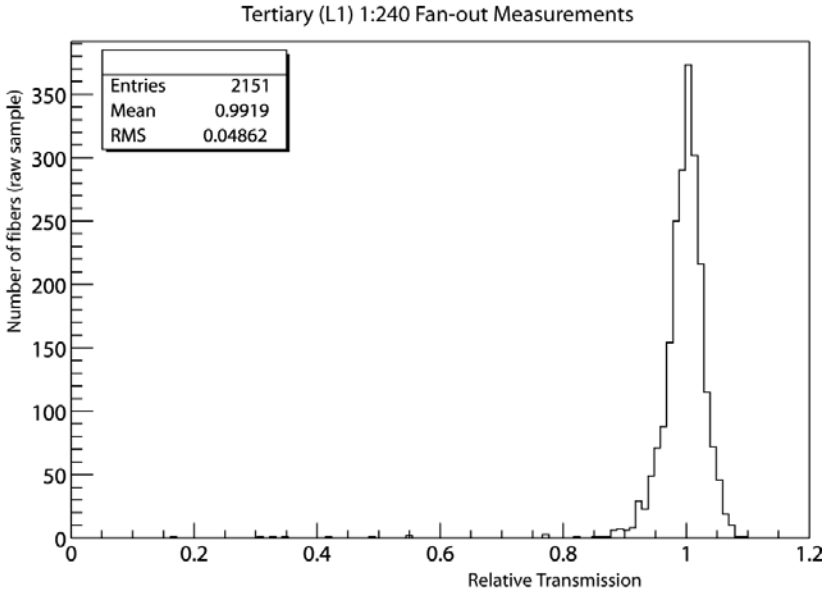

***Figure 24**. Typical tertiary 240-fiber fan-out optical (632 nm) transmission results (means normalized): individual fiber's relative transmissions are plotted here for all of the 9 fan-outs of SM15.*

4.2. Front-end ASIC preamplifier characterization.

Each ASIC preamplifier is characterized in a dedicated test bench prior to its installation in a FEM unit. In addition to validating the functionality of the ASIC, precision measurements are performed of the capacitance of each of the two channel's C_{inj}, as well as a determination of the noise and linearity in the two gain ranges, and the cross-talk between channels. Care has been taken to avoid contamination of the low level signals from ground loops, switching charge injection, etc. Bi-stable low switching energy (3 μV) ASX22006 NAIS - Matsushita latching relays with gold-clad Ag-alloy contacts are used on the test circuit board to select input channels and two different output ADC ranges, thereby ensuring routinely reproducible measurements.

The C_{inj} are determined from the ratio of the respective transfer functions measured independently 1) via the signal input with an external reference capacitor of 2.223 or 2.253 pF, channels 1 or 2 respectively, and 2) via the V_{inj} internal calibration circuit. In the first case, a Wavetek 395 synthesized waveform generator is used to measure the response over the full operating range. In the second case, an AOIP SN8310 DC voltage/current calibrated source is used to provide the V_{inj} levels with a precision of 0.002%; the individual DC voltage values used for the linearity and capacitance measurements were validated with a French COFRAC certified calibration. The stability of this source is better than 0.004% over a year. In both cases, the output signals are digitized with a CAEN C205A 12-bit charge integrating ADC and the slope of the transfer function is determined from a linear fit over 10 points (equivalent V_{inj} values gain A are from 20 mV to 1200 mV, and gain B are from 500 mV to 5 V). Each point represents the mean of 1000 measurements. The final slopes are separately averaged over 5 runs, and the C_{inj} is given by the ratio of the two slopes, results are shown in Fig. 25. The short term reproducibility between measurements on the bench is $\pm 2 \cdot 10^{-4}$ pF. The reproducibility of C_{inj} measurements for the same front-end ASIC re-measured after a month is $\pm 6 \cdot 10^{-4}$ pF.

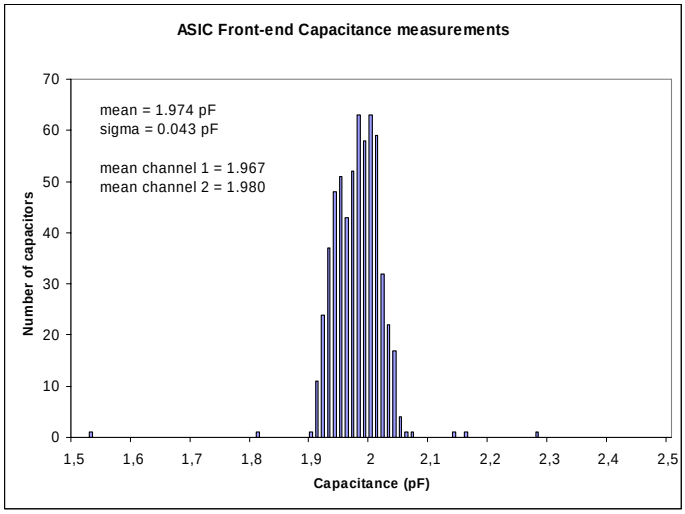

Figure 25. *Front-end ASIC internal capacitance C_{inj} measurements. Values are typically within ± 2.2% RMS.*

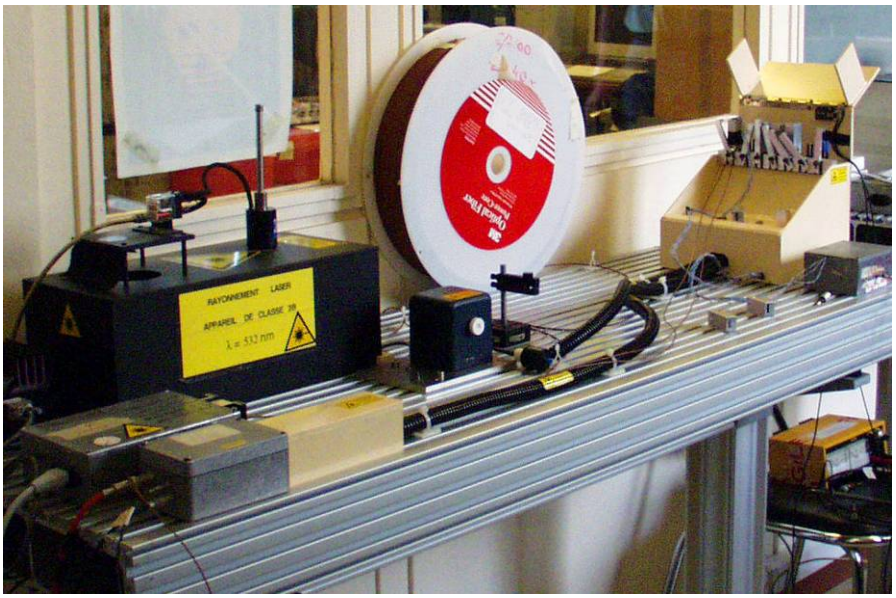

Figure 26. *The FEM unit characterization bench. The 4 FEMs under test, along with 2 reference FEMs, are mounted in the housing at the right.*

4.3. FEM unit characterization.

All FEM units were characterized on a dedicated bench in a temperature controlled room (18 ± 0.5°C) shown in Fig. 26. Groups of 4 FEM units were tested together along with a two reference FEM. Quantum efficiencies were measured at three wavelengths with separate sources: at 450 nm with a blue LED, at 532 nm with a green laser, and at 660 nm with a red diode laser. Results are shown for a sub-sample in Fig. 27. The measured quantum efficiency spread was within 1% RMS. The typical mean values are respectively 62%, 64% and 65%. Two measurements were performed at each wavelength before the burn-in discussed in sect. 4.4 and one afterwards as a cross-check. Units which showed deviations between the first two measurements ≥1% in any wavelength were rejected. This selection affected 1% of the FEM units.

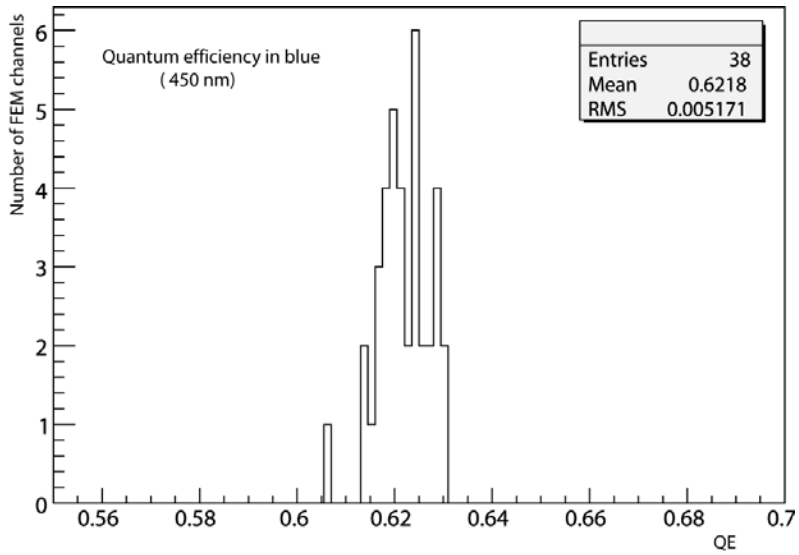

Fig 27. *Typical quantum efficiency results for a sub-sample of FEM units measured on the characterization bench: the mean value at 450 nm (blue) is 62.2% with an RMS spread of 0.8%.*

4.4. FEM unit burn-in and tests before installation.

In order to ensure the reliability of the FEM units before their final installation, we performed a week long burn-in on each device at 60° C, with laser light monitoring at 532 nm every 30 min. This tests both the PN photodiodes and their electronics. The measurements are performed by batches of 8 FEM units, testing 16 PN photodiodes simultaneously. The laser light is distributed to each FEM using a spare tertiary L1 fiber-optic fan-out and diffusing sphere. A channel's signal is normalized against that from a common reference photodiode for the batch, and the resulting ratio PN_i/PN_{ref} is followed over the burn-in period. A drift of ≥ 0.5% in the ratio is classed as a pathological device. As an example, Fig. 28 shows a typical result of a burn-in procedure for 2 diodes, one "acceptable" and one "pathological" rejected for installation.

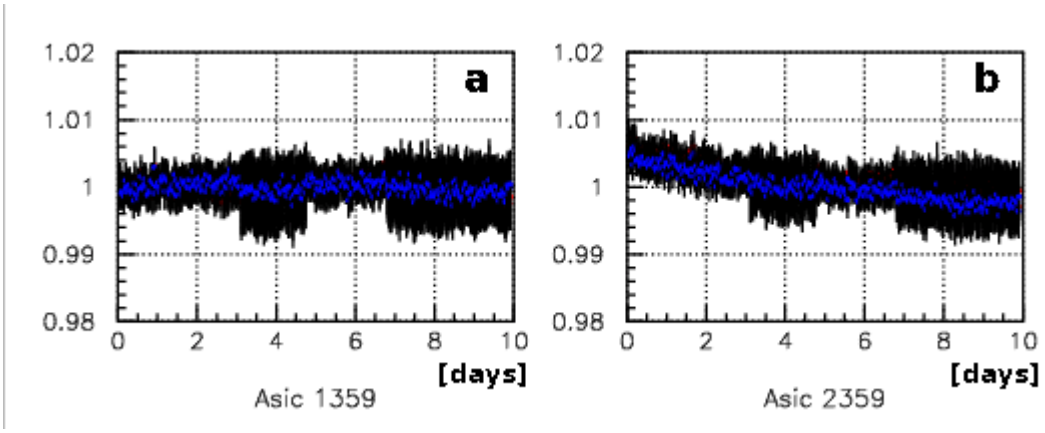

Figure 28. *Typical FEM burn-in results for the relative signal amplitude PN_i/PN_{ref} for laser light at 532nm: acceptable behavior over 10 days (a) versus pathological behavior over similar period (b).*

Altogether 1% of assembled FEM units were rejected after burn-in. Follow up on these units confirmed previous results from the R&D phase: failures are primarily concentrated on the PN photodiodes and not on the PCB and ASIC chips. The problem with the PN photodiodes appears to be related to a minor defect in the quartz window bonding. It is suspected that subsequent air intrusion affects the sensitive surface resulting in response drifts with time.

Although difficult to identify and reject microscopically before FEM assembly, this defect is clearly observable during the accelerating aging burn-in procedure.

4.5. Installation on ECAL barrel SM.

The on-board components of the monitoring system for each of the 36 ECAL barrel SM are installed at the end of the "bare" SM assembly, see Fig. 29. This is done prior to closure of the SM's front face, while the SM is still on its rotating assembly frame at the CERN Meyrin site. Altogether 1700 crystals/SM must be individually equipped with optical fibers and the reference PN photodiode sub-system must be installed and validated. The finished "bare" SM is then transported to the electronics installation hall at the CERN Prevessin site where the calorimeter is equipped with its Front-End electronics and undergoes a full check-out. This bi-phase assembly places two main constraints on the monitoring installation: 1) the assembly rhythm directly depends upon the monitoring installation time, and 2) monitoring system must be fully debugged before the transport.
The full monitoring installation has been limited to 10 working days/SM by using a team of 4 technicians, working by pairs on alternate sub-modules (adjacent sub-modules are covered to avoid accidental damage) once all of the FEM units and optical-fiber guides have been glued into the front face (SM positioned with the front face up). Specially adapted surgical pliers are used to insert individual optical fiber ferrules into the ferrule supports (a particularly delicate operation for the highly tilted crystals, ~60° from vertical, in module 4). The routing of the front face water cooling plumbing complicates this task. Poorly inserted or broken fibers require interventions at $\leq 0.5\%$ level, which is equivalent to the number of interventions required for trapped dust particles or unclean ferrules. This low frequency of interventions allows delaying the system check-out until the insertion phase is completed. The SM is then rotated (face down) and a 10-channel amplifier card is plugged sequentially into each of the APD signal connectors. A 532 nm (green) JDS Uniphase [24] NanoGreen 3 μJ laser located at the SM and running at 3 kHz is used to send pulses to crystals via the monitoring system. The APDs are operated without bias voltage, since the photocurrent is sufficient. The charge integrated and amplified APD signals are evaluated on a scope: badly inserted ferrules, broken fibers, or dust particles give signals $\leq 50\%$ and unclean ferrules give $\leq 75\%$; both cases are easily identified and repaired (typically 10 spare fibers are available per tertiary fan-out). The reference PN photodiode system is verified with an electronic test pulse and with the laser signals. Once validated, the SM is rotated again front face up and the upper layer of front-face water cooling is installed. Next the neutron moderator polyethylene beads are poured into the space around the fibers and the sub-module covers are mounted. The SM is again rotated face down and a final test of all channels is performed before transport to the electronics installation hall. The final element of the monitoring electronics chain, the MEM read-out module, is installed on the SM at the end of the electronics installation at the CERN Prevessin site. The full system is then validated using a 523 nm (green) Q-switched Opton [25] Nd:YLF 30 μJ laser (FWHM < 13 ns, jitter ≤ 0.2 ns).

Figure 29. *Installation of the monitoring distribution system on an ECAL barrel SM: (a) shows tool used to insert the optical fiber's ferrule into a crystal's ferrule support, (b) shows the 10-channel amplifier and connector used to test APD response after cabling (SM face down), and (c) shows the installation of optical fibers on alternate sub-modules (SM rotated front-face up).*

4.6. Installation on ECAL end-cap Dees.

The installation of the monitoring system on the end-cap differs from the barrel due to the modularity of the SCs (5x5 crystals) which are individually mounted on the back-plate of the end-cap Dee. As a consequence, the HV cables, signal cables and tertiary level optical fibers must be installed from behind each SC via access slots in the back-plate. Prior to the cabling and installation of the SCs, all of the monitoring system components (secondary and tertiary fan-outs, FEM units, bus-lines, etc.) are pre-installed on the rear of the back-plate. Due to the

space taken by the forward neutron moderator which shields the EE electronics, all of the monitoring components, except the optical fibers, are positioned at radii > 1300 mm. The cabling and installation of the tertiary fibers for each SC is performed when it is positioned near the final position with the SC loader arm, as shown in Fig. 30. Once the fibers are installed and the SC is bolted in place, the excess optical fiber (~30 cm) is pulled through the slot and fastened on the rear of the back plate, as shown in Fig. 31a. Validation of all optical connections is performed with a portable LED light injection and readout system; this operation must be performed just before attaching the SC to the base plate due to the inaccessibility of the fiber ferrules afterwards. The complete installation of the light distribution system, see Fig. 31b, requires 8 weeks per Dee.

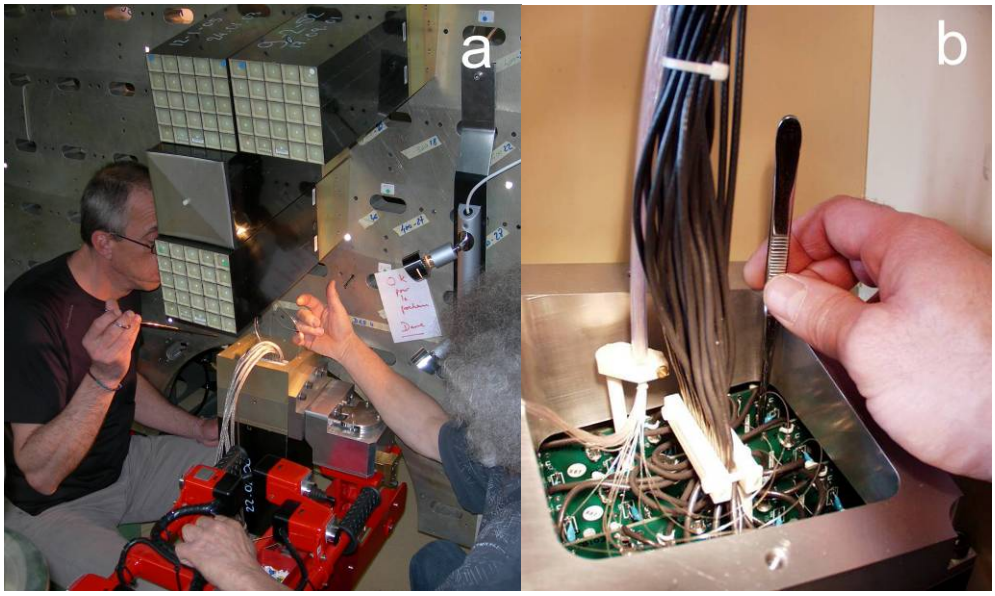

Figure 30. *Installation of tertiary (L1) fibers on an end-cap SC. In (a) the SC is positioned face down ~ 30 cm below its final mounting position with the SC loader arm to allow the insertion of the fibers (4 SC mounted on the back-plate can be seen above). In (b) a detailed view from the mock-up studies shows the fiber being inserted in to the rear of the SC through spaces between the HV PCB.*

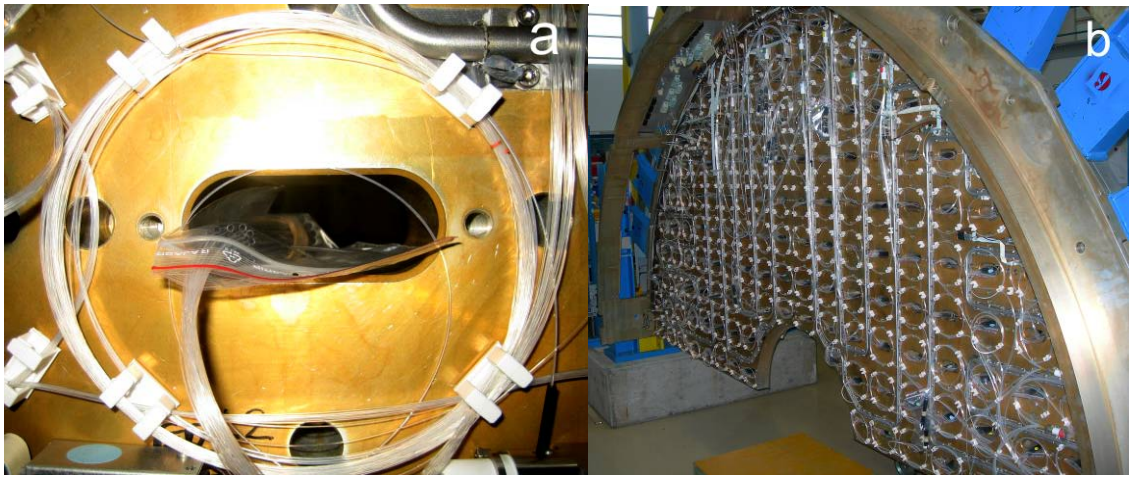

Figure 31. *Rear view of the end-cap back-plate. In (a), once the SC is bolted in place on the front-side, the excess length of tertiary fibers are retracted and fastened around the access slot. In (b) one can see the fully installed light distribution system on the back-plate.*

Figure 32. *SM mounted on automated scanning table in CERN H4 electron test beam.*

5. Laser monitoring system performance

5.1. CERN H4 test beam runs and set-up

We have evaluated the stability of the final laser monitoring system in test-beam runs at CERN on partially equipped SMs in 2003 and on fully equipped SMs in 2004. The CERN SPS H4 secondary test beam facility supplying narrow momentum bite electron beams from 20 to 250 GeV/c was used. Typical beam momentum spread is 0.09% with an additional contribution from synchrotron radiation fluctuations at momenta above 120 GeV/c (typically 0.11% at 180 GeV). The H4 beam allows irradiation studies using high rates (> 2000 electrons per burst). First results of calorimeter performance have been published elsewhere [26]. The data presented here were taken with supermodule SM10 in runs of 120 hrs and 360 hrs in autumn 2004. In addition, subsystem elements have been evaluated in prototype tests for periods up to 700 hrs.

Any one of the SM's crystals can be irradiated at the test facility using an automated rotating scanning table shown in Fig. 32. The setup is designed to reproduce the incident geometry for photons produced at the LHC interaction point. The incident electron position was defined by a set of hodoscopes. Readout of the calorimeter was triggered by electrons passing through a 5x5mm^2 plastic scintillator placed in front of the targeted crystal.

Irradiation runs at 120 GeV/c and dose rates of 0.2 to 0.4 Gy/h lasted 10 hours; during a typical 0.2 Gy/h irradiation about 30 000 electrons enter a crystal face per SPS spill. Typically 40 SPS spills at 120 GeV/c, but lower intensity (3000 electrons per spill), were used for "electron runs" to measure a crystal's energy response. These were alternated with "laser runs" consisting of 1200 laser pulse triggers (100 Hz) and 40 electronics test pulse triggers, giving a monitoring point every 20 minutes. Pedestal runs were performed at the same rate.

The stabilities of two operating parameters are critical to the performance of the SM at the test beam: temperature and high voltage. In the first case, both the $PbWO_4$ crystal's scintillation yield and the APD gains are strongly temperature dependent with a typical global response variation of -4%/° C. A large effort has gone into designing an 18° C cooling

system which can maintain the mean temperature spread below 0.05° C. This issue under the test beam conditions at H4 is addressed at some length in ref. [26]. Concerning the high voltage stability, the APD gain is strongly dependent upon the bias voltage (1/M dM/dV ≈ 3.2%/V at a typical gain M of 50). A CAEN prototype of the final system HV supply was used for the tests, providing a dispersion within specifications of less than ± 20 mV at 500 V.

5.2. Laser source performance and operation at test beam facility

The first laser system was installed at the CERN H4 test beam site in 2001, followed by the other two in 2003. More than 20 000 laser hours have been cumulated in the ECAL test beam program. This experience confirmed the need for a clean environment with class better than 10 000. In 2005, three portable clean room facilities were installed at H4, providing a clean environment of better than class 1 000 for laser optics protection. In this section two essentials of the laser system performance are addressed: environmental temperature and Nd:YLF pumping laser stability, additional details may be found in ref. [27].

The environmental temperature dependences of the Ti:Sapphire laser pulse energy and width were initially measured at Caltech. Since the installation at the test beam lacks the ≤ 0.5° C stability foreseen for the LHC laser barracks, this issue is important for the precision of the tests discussed here. The temperature slopes of the pulse energy, FWHM and timing were found to be -4.3%/°C, 1.3 ns/°C and 7.9 ns/°C respectively. Under test beam operating conditions this leads to short term RMS spreads of typically 1% to 2% over 30 minutes in the laser pulse energy (E_{pulse}) and FWHM width (Γ_{pulse}), where the corresponding pulse jitter is less than 2 ns. Runs over periods of more than 24 hours show spreads of about 3% at 440 nm (blue) and 796 nm (near IR), and about 7% at 495 nm (green) and 709 nm (red), where the narrower spread at the first two wavelengths is due to more stable operation near the Ti:Sapphire's emission peak at 800 nm (FWHM 120 ns) or its frequency doubled value.

The stability of the Nd:YLF pumping laser used in each of the three sources plays a key role in the stability of the corresponding Ti:Sapphire laser's pulse energy (E_{pulse}), width (Γ_{pulse}) and timing (t_{pulse}). If the Nd:YLF pumping current is held at a fixed value, a degradation of the stability and a drift of the laser pulse timing at the level of 2ns/day are observed for runs longer than 24 hours. This is due to the aging of the DC Krypton pumping lamp, which is normally replaced after 1 000 hours of operation after about 10% laser pulse energy loss. The slopes between the Nd:YLF pumping current I and the Ti:Sapphire laser pulse energy, width, and timing were measured at Caltech for a pumping current of 25 A, giving respectively: $\Delta E_{pulse}/\Delta I$ = 0.09 mJ/A, $\Delta \Gamma_{pulse}/\Delta I$ = -1.7 ns/A, and $\Delta t_{pulse}/\Delta I$ = - 46 ns/A. This long term variation can be compensated by incrementally increasing the YLF pumping current via the laser control and DAQ program. This technique was implemented in 2006 using software feedback, where the laser pulse timing is used as the feedback parameter [28]. The results for several laser runs with a total combined running time of 650 hours give both pulse energy and FWHM stability at the 3% level and a pulse timing jitter of 2 ns.

5.3. Data treatment and normalization.

The laser light signal from each crystal's pair of APD is shaped and digitized at the 40 MHz LHC clock rate (10 samples recorded, sampling rate every 25 ns). Pedestals are defined for each crystal's channel using the mean of the first 3 digitized samples ahead of the laser signal. This value is then subtracted from the subsequent laser signal before the pulse amplitude

reconstruction. The maximum amplitude is obtained using a parameterized fit function, which reproduces the APD electronics response given by the formula:

$$A(t) = A_0 \left(\frac{t - t_0}{\beta} \right)^{\alpha} e^{-\alpha \left(\frac{t - t_0 + \beta}{\beta} \right)},$$

where β is the electronics decay time, and the product α·β is the electronics rise time. The two fit parameters α and β are adjusted using the 3 samples nearest the maximum sample found (i.e. one sample before maximum and two samples after maximum), typical values are 1.41 and 39.25 ns (α and β respectively). Fig. 33 shows typical APD responses for different laser pulse-widths.

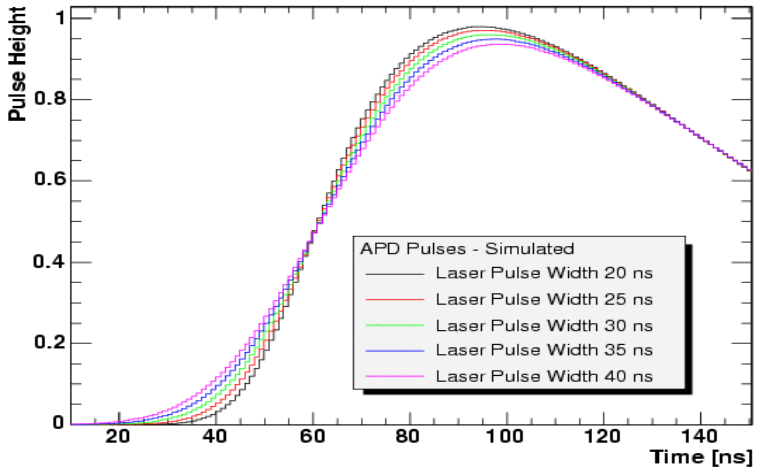

Figure 33. *Simulated APD pulse shape for different (Gaussian) laser pulse-widths: 20, 25, 30, 35, and 40 ns.*

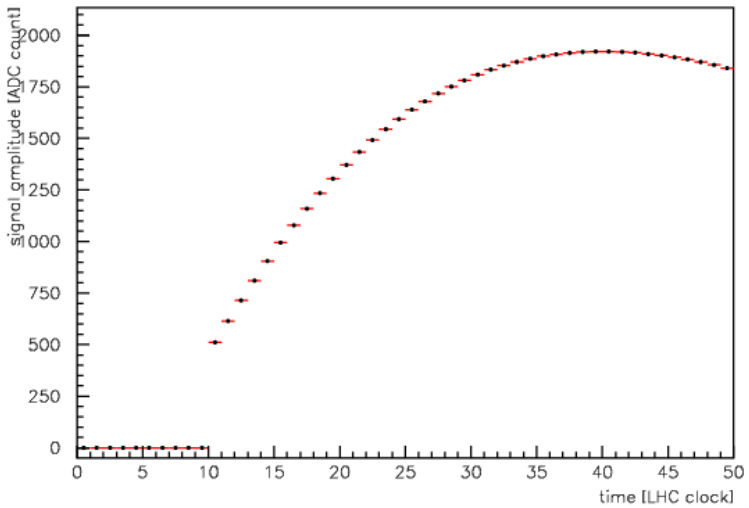

Figure 34. *Typical PN pulse shape (LHC clock rate is 40MHz). PN pulse shape is not significantly affected by variations in the laser pulse-width in the 20 to 40ns range.*

The response of the reference PN photodiodes sharing the same tertiary fiber-optical fan-out as the crystals, shown in Fig. 34, is much slower due to the 1.16 μs shaping discussed earlier. The signal is digitized in 50 samples at 40 MHz, and the maximum response is determined by

a 2nd degree polynomial fit using 16 samples around the maximum sample found, where the pedestals, defined using the mean of the first 5 samples, were previously subtracted.
The normalized laser response APD/PN of each channel is obtained by dividing its APD maximum amplitude by the commonly shared PN maximum amplitude on an event by event basis. Afterwards, an average of the 1200 events for the laser run is computed.

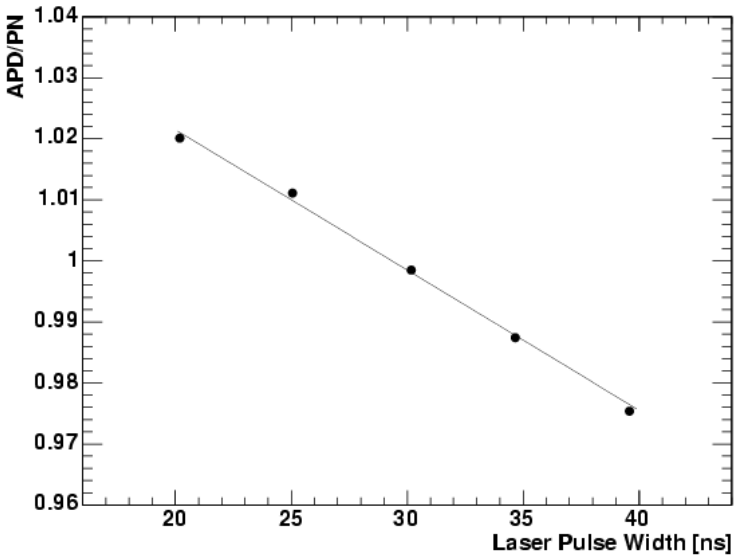

Figure 35. *Ratio APD/PN response versus laser pulse-width for simulated Gaussian laser pulses and fixed APD response parameters α and β.*

5.3.1. Data corrections.

Several corrections at the 0.05 to 2% level are required to use the raw laser response averages, and these are discussed below:

1) Laser pulse-width variations: Fig. 35 shows the dependence of the laser response APD/PN versus laser pulse-width for a given set of values α and β. Unfortunately during the beam tests discussed here the CAEN V1729 switched-capacitor digitizer was not yet implemented (decision to implement this unit was based upon these results). In order to determine laser pulse-width changes we followed the rise time stability run by run using the APD fit parameters for selected channels (one per each 5 x 5 channel trigger tower), inferring the pulse-width from the rise time. Corrections in APD/PN response using the curve in Fig. 35 were "smoothed" by requiring that 75% of the selected channels on the half of the SM receiving the laser pulses showed ≥ 0.5% change in the rise time before correcting all of the associated channels. In practice, laser stability was sufficiently good such that these corrections were required only about once per week; typical corrections are at the 0.05% level.

2) Electronics gain correction: Test pulse charge injections using the charge injection system located on each FEM, coupled to an AOIP SN8310 DC voltage/current calibrated source, were performed during each laser run. Since electronics gain drifts are expected on time scales much larger than 20 minutes, only 40 test pulse events were taken per laser run. Measured dispersion for PN response under test beam conditions is typically 0.26%. Corrections were applied when the gain

change was ≥ 0.04%. In practice this was ≤ 1% and only concerned the first few hours of startup after a machine shut-down.

3) Correction for gain non linearities: the measured PN amplitude can be separated in two parts, a linear part and a non linearity correction:

$$PN_{meas} = \alpha\, Q_{PN} + \delta\, PN,$$

where Q_{PN} is the charge at the entrance of the preamplifier. In case of light injection, $Q_{PN} = \varepsilon_q \; n_\gamma$ with ε_q the quantum efficiency of the PN diode and n_γ the number of photons received by the PN diode. In case of charge injection,

$$Q_{PN} = Q_0 + C_{inj}\, V_{inj},$$

where C_{inj} is the ASIC's (~ 2 pF) internal injection capacitor (see sect. 2.6.1), and V_{inj} the external injection voltage. Q_0 is the parasitic charge injected by the switching system itself which appears in Fig. 36a (inset) as a shift in the injection voltage (~ 1 mV). The non linear correction is a curve obtained by subtracting the measured response from a linear gain curve, where we assume $\delta PN = 0$ at $Q_{PN} = 0$ and arbitrarily define that $\delta PN = 0$ for $V_{inj} = 600$ mV. A typical non linearity curve is shown in Fig. 36b. Such curves are measured in dedicated runs and are found to be quite stable. The results are parameterized by a 3rd degree polynomial function which is subsequently applied to correct the measured PN signals. The maximum correction is obtained for signal amplitudes around 1300 ADC counts and is of the order of 2%.

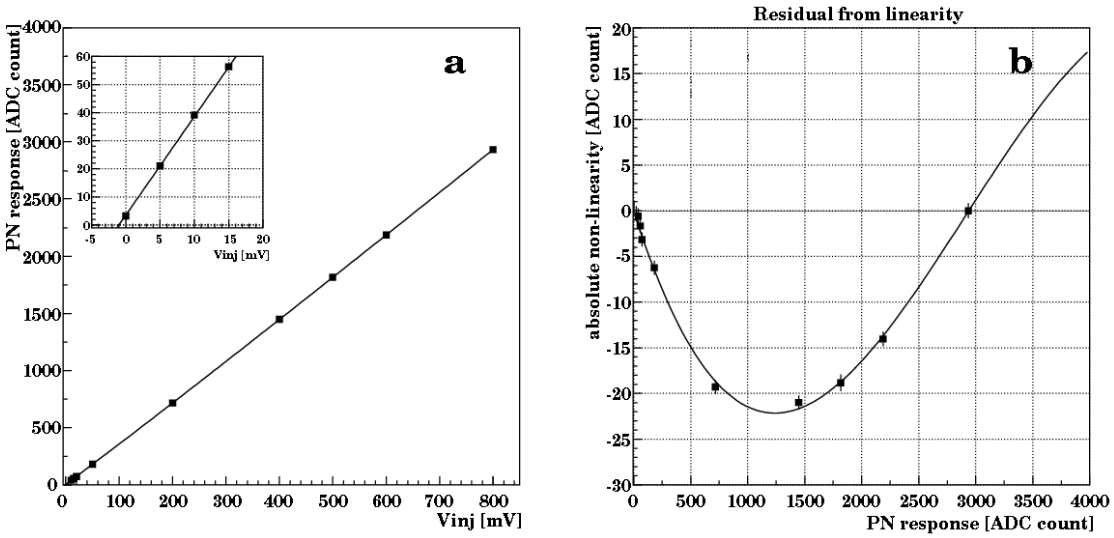

Figure 36. *PN linearity measurements: (a) PN response versus injection voltage, V_{inj} (inset shows results for values of $V_{inj} \leq 15$mV), and (b) residual non-linearity is plotted in ADC counts over the full range.*

5.4. Monitoring stability results

First, we verify the stability of the light calibration system for each group of 200 crystals using the relative stability of the associated pair of reference PN photodiodes. The measurements of the ratio of the two PN responses, determined on an event by event basis and averaged over each run, are plotted together in Fig. 37 for 104 laser runs taken over a period of 7.5 days. The results demonstrate that the system achieves an RMS spread of 0.0074% over this period.

Next, we verify the stability of the response to injected laser light at 440 nm (blue) for a group of non-irradiated crystals using the normalized laser response APD/PN determined for each

laser run as discussed in sect. 5.3. This ratio is called the relative crystal transmission. A group of non-irradiated crystals located in the left half of SM10's module 1 were chosen. The APD/PN ratios are plotted for each of the 200 crystals over 11.5 days of operation in Fig. 38. The figure shows that a stability of 0.068% has been achieved over this period.

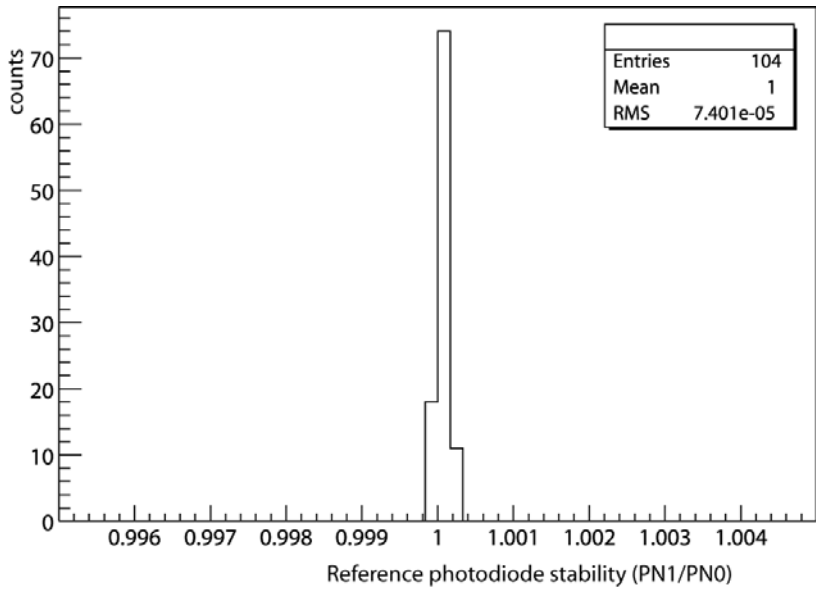

Figure 37. *Relative stability between pair of reference PN photodiodes monitoring 200 crystals (SM 10 module 3) measured in autumn 2004 at the CERN test beam facility. RMS spread over 7.5 day's operation (104 laser runs) is* $0.74 \cdot 10^{-4}$.

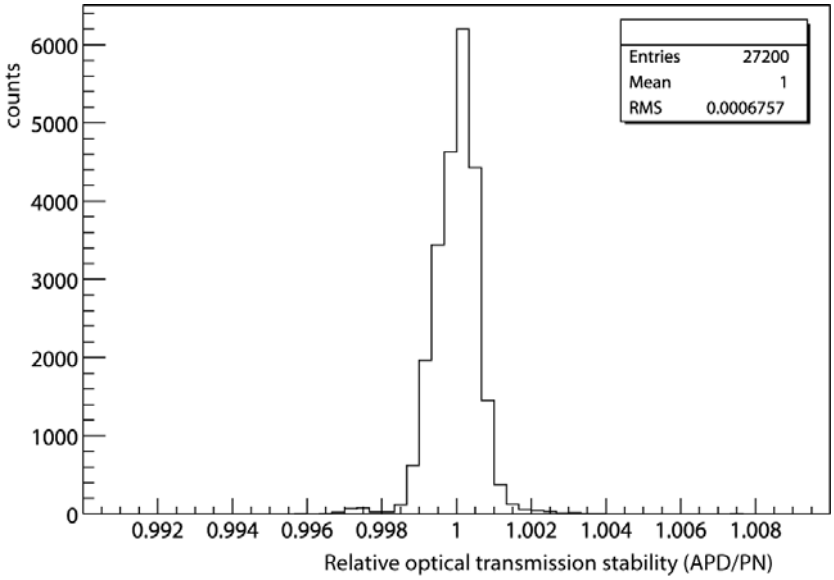

Figure 38. *Stability of crystal transmission measurements at 440 nm (blue) over 11.5 day's operation (136 laser runs) at CERN test beam facility is* $6.76 \cdot 10^{-4}$ *RMS for a module of 200 non-irradiated crystals (SM 10 module 3).*

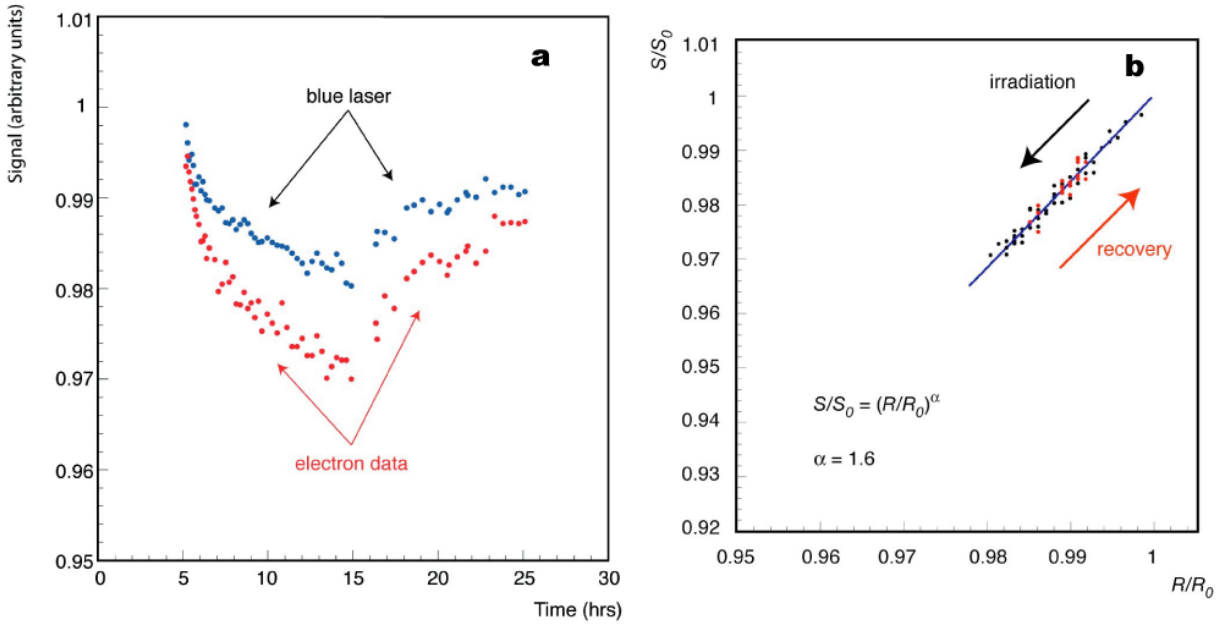

Figure 39. *Irradiation with 120 GeV electrons and recovery for a single $PbWO_4$ crystal (SM10): (a) upper curve shows APD response to laser injection at 440 nm (blue laser), and lower curve shows response to 120 GeV electrons; (b) plots the signal response S/S_0 against the laser response R/R_0 for the same data, where the line shows the fit for $\alpha = 1.6$.*

5.5. LHC-type irradiation test and crystal transparency energy correction.

Changes in the crystal transparency due to radiation damage do not affect the amplitude of the APD signal S for an electromagnetic shower in exactly the same way as it affects the APD signal for injected laser pulses R. This is principally due to different mean light paths in the two cases. The effect can be seen in Fig. 39a, shown previously in [26], where single crystal relative responses to both 120 GeV electrons S/S_0 (measured in low intensity electron runs) and to injected laser light from the monitoring system R/R_0 (measured in alternated laser runs) are plotted during an irradiation run at 0.15 Gy/h. The measurements were taken both during irradiation phase ending at 15 hrs in the figure, and during the subsequent recovery phase. The initial values S_0 and R_0 correspond to measurements taken prior to the irradiation. The relationship between the two responses can be modeled for small variations as

$$\frac{S}{S_0} = \left\{ \frac{R}{R_0} \right\}^{\alpha} .$$

The excellent agreement between this description and the data can be seen in Fig. 39b, where a fitted slope of $\alpha = 1.6$ is superimposed on the data. Data taken during irradiation and recovery phases follow the same slope. Typical fit precision is 3%, and the intrinsic dispersion for the crystals is deduced to be about 6%. At LHC this relationship allows the monitoring system to correct for transmission losses. Thus for crystals showing a decrease in signal size of 5% a single value of α can be used to correct the loss, with a precision of 0.3%.

6. Summary

A multiple wavelength laser monitoring system for the CMS ECAL has been designed and constructed: the monitoring light source, diagnostics, and high level distribution system at Caltech and the calorimeter light distribution system, reference PN photodiode system, and

associated electronics at CEA-Saclay. The system was commissioned and validated at the CERN test beam facility; the measured performance of 0.068% stability in optical transmission measurements at 440 nm (blue) over 11.5 days demonstrates the system's capability to achieve ≤ 0.2% drift/month stability required for precision crystal calorimetry at the LHC.
Installation of the monitoring system on the barrel calorimeters was finished in June 2007, and the completion of the installation on the end-cap calorimeters is foreseen for April 2008.

Acknowledgements

The authors would like to thank the CMS ECAL collaboration, especially E. Auffray, P. Ingenito, P. Lecoq, M. Lebeau, O. Teller, J. Greenhalgh, J. Hill, A. Lodge, B. Smith, R. Benetta, and M. Hansen. We thank particularly J. Bourotte and M. Haguenauer for their effort at the test beam facility; the Saclay team thanks E. Pasquetto and D. Pierrepont for their help at CERN, and D. Bederede, D. Loiseau, and F. Rondeaux for their help at Saclay.

References:

[1] "The Electromagnetic Calorimeter Technical Design Report," CMS Collaboration, CERN/LHCC 97-33, 1997.
[2] R.Y. Zhu, *Nucl. Instr. and Meth.* **A 413** (1998) 297.
[3] A. Annenkov, *et al. Phys. Stat. Solids* **A 191** (2002) 277.
[4] P. Azdic *et al*., "Energy Resolution of the Barrel of the CMS Electromagnetic Calorimeter", *JINST* **2** (2007) P04004.
[5] B. Adeva *et al, Nucl. Instr. and Meth.* **A289** (1990) 81.
[6] OPAL Collaboration, *Nucl. Instr. and Meth.* **A305** (1992) 293-295.
[7] Y. Kubota et al., *Nucl. Instr. and Meth.* **A320** (1992) 96-97.
[8] B. Aubert et al., *Nucl. Instr. and Meth.* **A479** (2002) 78.
[9] V.A. Batarin *et al.*, *Nucl. Instr. and Meth.* **A534** (2004) 486.
[10] E. Auffray, *et al. Nucl. Instr. and Meth.* **A 412** (1998) 223.
[11] "The Large Hadron Collider Conceptual Design", CERN/AC/95-05 (LHC) (1995), P. Lefevre and T. Peterson, ed.
[12] Appendix A: "Radiation environment" ref [1].
[13] L.Y. Zhang, *et al. IEEE Trans. Nucl. Sci*. **NS-48** (2001) 372.
[14] Quantronix, 41 Research Way, East Setauket, NY 11733 USA.
[15] DiCon fiberoptics, Inc., 1689 Regatta Blvd. Richmond, CA 94804. Email: info@diconfiber.com.
[16] D. Breton and E. Deslagnes, "Very high range and high sampling rate VME digitizing board for physics experiments", Proceedings 10TH Workshop on Electronics for LHC experiments and future experiments, Boston (2004), CERN 2004-010.
[17] Epoxy EPO-TEK 353ND.
[18] SEDI fibres optiques, 6 rue Jean-Mermoz, Z.A. de St Guénault, 91080 Courcouronnes, France. Email : info@sedi-fibres.com.
[19] Spectralon®, Labsphere, Inc., North Sutton, NH 03260 USA.
[20] M. Hansen, "The New Readout Architecture for the CMS ECAL", Proceedings 9TH Workshop on Electronics for the LHC Experiments, Amsterdam (2003), CERN 2003-006.
[21] K. Gill, et al. "Gamma and neutron radiation damage studies of optical fibers", *Journal of Non-crystalline Solids*, **216** (1997) 129.

[22] N. Akchurin, *et al*. “Preliminary results from *in situ* quartz fiber neutron irradiations”, CMS NOTE 1998-056.
[23] P. Denes, *et al. “Radiation hardness evaluation of the Analog Devices AD9042 ADC for use in the CMS electromagnetic calorimeter”, Nucl. Instr. And Meth.* **A 417** (1998) 371.
[24] JDS Uniphase, 430 N. McCarthy Blvd., Milpitas, CA 95035 USA.
[25] Opton laser International, Parc Club d’Orsay Université, 29, rue Jean Rostand, 91893 Orsay Cedex France.
[26] P. Adzic, *et al. Eur. Phys. J*. **C 44**, Supplement 1 (2006).
[27] L. Zhang, *et al. , IEEE Trans. Nucl. Sci.* **NS-52** (2005) 1123.
[28] L.Y. Zhang *et al*., “Implementation of a Software Feedback Control of the CMS Monitoring Lasers”, *IEEE Nucl. Sci. Symposium Conference Record* (2006).